

Banner appropriate to article type will appear here in typeset article

Theoretical analysis of stress perturbations from a partially-lubricated viscous gravity current

Joshua H. Rines^{1,2} †, Ching-Yao Lai^{1,2} and Yongji Wang^{1,2,3}

¹Department of Geophysics, Stanford University, Stanford, CA

²Department of Geosciences, Princeton University, Princeton, NJ

³Department of Mathematics, New York University, New York, NY

(Received xx; revised xx; accepted xx)

We present a theoretical investigation into the dynamics of a viscous gravity current subjected to spatially-finite lubrication (i.e., a ‘slippery patch’). The work is motivated by grounded ice sheets flowing across patches of basal meltwater which reduce the ice-bed frictional coupling, causing perturbations enhancing ice motion, with implications for increased ice flux into the ocean and sea level rise. The flow is characterized by transitions between shear- and extension-dominated dynamics, which necessitates boundary-layer solutions at the transition points. We develop a depth-integrated analytical model of Newtonian flow which concisely reveals fundamental relationships between ice sheet geometry (thickness, surface slope, and slippery patch length) and the magnitude and spatial extent of resulting horizontal deviatoric stresses. This reduced-order analytical model shows good quantitative agreement with numerical simulations using 2-D Newtonian Stokes equations, which are further extended to the case of a non-Newtonian flow. From the reduced-order model, we rationalize that the slippery patch-induced stress perturbations are exponentially-decaying functions of distance upstream away from the patch onset. We also show that the amplitude of the perturbation scales linearly with the surface slope and patch length while the decay lengthscale scales linearly with ice thickness. These fundamental relationships have implications for the response of the Greenland Ice Sheet to the inland expansion of basal meltwater presence over the coming warming decades.

Key words: Authors should not enter keywords on the manuscript, as these must be chosen by the author during the online submission process and will then be added during the typesetting process (see [Keyword PDF](#) for the full list). Other classifications will be added at the same time.

MSC Codes (*Optional*) Please enter your MSC Codes here

† Email address for correspondence: jrines@stanford.edu

Abstract must not spill onto p.2

1. Introduction

The flow of glacial ice, such as the Antarctic and the Greenland Ice Sheet (GrIS), is broadly divided into two regimes: (1) extension-dominated plug flows and (2) shear-dominated flows. The former describes ice flows which are subjected to negligible or relatively small tangential traction on the basal boundary, such as ice streams and ice shelves. Ice streams are narrow regions of grounded ice which flow rapidly over low friction beds (Rink 1877; Swithinbank 1954; MacAyeal 1989; Leung & Kowal 2022), while ice shelves are floating extensions of ice sheets that cross the grounding line, the boundary between grounded and floating ice (Weertman 1957; Morland 1987; MacAyeal & Barcilon 1988). The latter regime (shear-dominated) describes grounded ice with strong frictional coupling between the ice and the bed, such as GrIS flow in the winter (Zwally *et al.* 2002; Stevens *et al.* 2016). The interfaces between these two regimes are critical to ice sheet evolution under the warming climate. For example, the organization of ice flow into ice streams, which serve as fast-flowing conduits through which Antarctic ice is rapidly transported seaward (e.g., Bindshadler & Vornberger 1998; Hulbe & Fahnestock 2007; Rignot *et al.* 2011), is dependent on the dynamics associated with a transition between shear- and extension-dominated regimes (Clarke *et al.* 1977; Yuen & Schubert 1979; Mantelli *et al.* 2019). In addition, unstable grounding line retreat (and therefore increased ice mass flux into the ocean contributing to sea level rise) under a warming climate has been shown to depend critically on the dynamics at the grounding line transition between grounded and floating ice (Weertman 1974; Schoof 2007a). Another interface, which has received less analytical attention than the aforementioned analogues, is a seasonally-occurring feature of the GrIS flow system: rapid spatially-finite injections of surface meltwater to the ice-bed interface from drainage of supraglacial lakes through the ice column.

At leading order, the GrIS behaves as a thin shear-dominated viscous gravity current, deforming under its own weight. Using lubrication theory under a slender-body assumption, simple models of this system result in a nonlinear diffusion equation (Fowler *et al.* 1978; Morland & Johnson 1980; Hutter 1983). Closed by boundary conditions zero ice thickness at the ice front and global mass conservation, the nonlinear diffusion model yields a self-similar solution for the ice thickness (Halfar 1981; Huppert 1982; Hindmarsh 1990; Nye 2000; Bueler *et al.* 2005). During the summer months (June-September) the ice-bed interface of the GrIS becomes partially lubricated by surface meltwater which penetrates the ice column via surface-to-bed pathways (Alley *et al.* 2005; Das *et al.* 2008). These spatially-finite injections of meltwater reduce friction between the ice and bed below, leading to acceleration of the overlying ice (Joughin *et al.* 2013; Stevens *et al.* 2016). In many cases, stresses induced by this acceleration are sufficient to trigger vertical propagation of water-filled fractures, causing the drainage of supraglacial lakes from the surface to the ice-bed interface (Das *et al.* 2008; Stevens *et al.* 2015; Poinar & Andrews 2021).

Rapid lake drainage via hydrofracture induced by basal traction loss (henceforth ‘rapid lake drainage’) delivers large volumes ($\sim 0.05 \text{ km}^3$) of surface meltwater to the bed (Fitzpatrick *et al.* 2014). This enhanced ice-bed lubrication has been shown, through observations and modeling, to impact ice dynamics on timescales ranging from daily to decadal (Zwally *et al.* 2002; Joughin *et al.* 2008; van de Wal *et al.* 2008; Bartholomew *et al.* 2011; Hewitt 2013; Sole *et al.* 2013; Schoof 2010; Stevens *et al.* 2016). In some cases, multiple nearby lakes are observed to drain in a rapid sequential manner, leading to the hypothesis of domino-effect-like lake drainage cascades (e.g., Christoffersen *et al.* 2018), which could have the capacity to transiently overwhelm the evacuation capacity of the subglacial hydrological system, increasing ice motion (Schoof 2010). This is especially relevant as the presence of lakes is projected to expand inland over the coming decades in response to the warming climate

(Leeson *et al.* 2015; Ignéczi *et al.* 2016; MacFerrin *et al.* 2019). These inland regions are characterized by a subglacial hydrological system which may be more readily overwhelmed by meltwater injections, leading to a more sustained ice motion response to this forcing (Schoof 2010; Meierbachtol *et al.* 2013; Dow *et al.* 2014; Doyle *et al.* 2014; Poinar *et al.* 2015). Moreover some studies, such as Fitzpatrick *et al.* (2014) and Christoffersen *et al.* (2018), conjecture that the drainage of one lake may impact the stresses at another lake located as far as tens of kilometers apart, implying a far-reaching lengthscale, or ‘coupling length’, over which these draining lakes communicate. However, some field-based studies indicate that coupling lengthscales of stress perturbations in response to a lake drainage event may be limited to several ice thicknesses, or on the order of single kilometers (e.g., Stevens *et al.* 2024). Constraining the controls on rapid lake drainage therefore remains critical and incomplete. In this study, we aim to answer the following question: what are the fundamental theoretical controls on the magnitude and spatial extent of the stress response to basal traction loss?

Theoretical analyses of ice sheet responses to basal traction loss, and the merits thereof, have long been recognized. Weertman (1974) first called attention to the climate-sensitive dynamics at grounding line transition zones between grounded ice and floating ice shelves. Built upon by a number of studies which employ boundary layer-based theoretical frameworks for grounding line dynamics (e.g., Chugunov & Wilchinsky 1996; Schoof 2007*b,a*, 2012), the resulting so-called marine ice sheet instability theory uncovers potentially the greatest threat to ice sheet stability, particularly in West Antarctica. Flow regime transitions for fully grounded ice have been similarly analyzed, though less extensively. Barcilon & MacAyeal (1993) analytically described the steady-state flow of an ice stream over a transition in basal boundary condition from no-slip to free-slip. Mantelli *et al.* (2019) extended the analysis of a no-slip to free-slip (‘hard-switch’) transition by modeling the associated thermomechanical boundary layers which form near the bed in response. These studies analyzed steady-state ice flow over a single boundary condition hard-switch between no-slip and free-slip.

We note that previous theoretical attention has been paid to the problem of ice flow over spatially-finite basal heterogeneities (e.g., topography and/or friction), though no previous study has resolved the stress-geometry relationships as we aim to do. In particular, several studies discussed that over long (e.g., steady-state) timescales, the signal of basal heterogeneities may be transmitted longitudinally on the order of several ice thicknesses away from the location of the heterogeneity (e.g., Kamb & Echelmeyer 1986; Gudmundsson 2003; Sergienko 2013; Crozier *et al.* 2018). Though most of these studies focus on how basal features are expressed in the surface topography, the lengthscale over which information transmits from bed to surface is consistent with the findings from our idealized model. Venuleo *et al.* (2019) analyzes instabilities and velocity field perturbations in a gravity current flowing over a spatially-finite porous substrate. Stubblefield *et al.* (2021) employs finite element methods to study contact problems concerned with grounding line dynamics of cyclically filling/draining subglacial lakes. While these previous studies are relevant and related to the problem at hand, no model yet exists which synthesizes the impacts of a spatially-finite slippery patch on the glacial stresses.

In this paper, we develop a boundary layer-based model for gravity current flow over a finite-length slippery patch which elucidates the leading-order controls on the induced stress perturbations. The interface between ice and the slippery patch is set to be stress-free, with the remaining parts of the bed satisfying a no-slip condition (figure 1). This simplifying choice of basal boundary conditions permits the use of a depth-averaged (1D) flowline analytical model which naturally lends itself to a boundary-layer description of the fundamental perturbed stress structure. Though simpler in construction than 2D analytical formulations of similar transition problems (e.g., Chugunov & Wilchinsky 1996; Mantelli *et al.* 2019), the reduced-

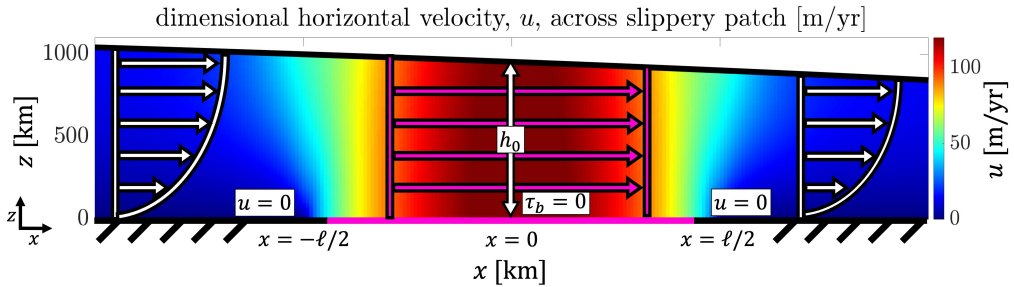


Figure 1: Geometry of ice flow from left to right across a bed characterized by no-slip (black) and a free-slip patch (pink); $h(x)$ is the ice surface, u is the horizontal velocity. This is an example of the simulation where the ice thickness is 1000 meters, the surface slope is 0.5 degrees, and the slippery patch is 10 km long. The horizontal arrows (not to scale) are to highlight the shear-dominated no-slip regions and the extension-dominated free-slip region over the patch. Note that all variables in this figure are dimensional.

order nature of our model reveals interpretable relationships between ice sheet geometry and perturbed stresses, specifically with respect to a finite patch of slip. Additionally, this simplifying case with a sharp slip to no-slip transition serves as an extreme end-member representation of the presence of basal sliding, which elicits the strongest stress perturbations. Overall, the novelty of our contribution is an analytical depth-averaged model derived from first principles which considers a finite-length slippery patch, revealing analytical structure of perturbed stress magnitude (τ_{xx}) and coupling length scale (CL) as a function of local ice thickness, surface slope, and the size of the slippery patch.

We begin, in §2, by deriving the 1D depth-averaged model for both the free- and no-slip regions. In §3, by implementing boundary layer theory and matched asymptotic analysis to connect the 1D models in both regions, we capture the stress structure in the transition zone between no-slip and free-slip. We validate the accuracy of this reduced-order model against numerical simulations, and extend the numerical analysis to 2D for a range of rheologies in §4. These analyses demonstrate a compelling consistency in the dominant controls on stress response. We conclude in §5 with a discussion comparing our model to previously-developed models and the implications of our findings for the GrIS under the warming climate.

2. Model development

We consider an along-flow two-dimensional ice sheet in a vertical plane (x, z) of constant viscosity flowing over a flat bed, where x is along the horizontal and z the vertical directions. The ice-bed interface is characterized by a no-slip condition everywhere, except for a free-slip region of finite length, ℓ , henceforward called the ‘slippery patch’ or simply the ‘patch’ (pink region in figure 1). The no-slip regions are governed, to leading order, by the balance between vertical shear stress and the horizontal gravity-induced pressure. In contrast, in the region interior to the patch, the vertical shear stress vanishes due to the absence of basal friction. Thus, the gravity-induced pressure is balanced by the horizontal extensional stress of the ice sheet. Considering the distinction of the dominant stresses inside and outside the patch, these two regions require separate treatment in developing an analytical model to describe the stress response. Importantly, we note that we are considering a system under which the surface topography does not have enough time to respond (relax) to the presence of the slippery patch, but where the patch may be present for long enough to elicit a viscous response. Namely, we consider a system operating under a timescale much shorter than the

relaxation time of the ice surface, ~ 100 days, but longer than the Maxwell timescale of ice, ~ 1 day (more on this in Appendix C).

2.1. Governing equations of 2-D flow

Let u, w be the velocities in the horizontal x - and vertical z -direction, respectively. The upstream onset of the slippery patch, $x = -\frac{\ell}{2}$, is the transition between no-slip and free-slip basal boundary condition, while $x = \frac{\ell}{2}$ is the downstream end of the patch and a transition back to a no-slip bed. The ice surface is denoted as h and the bed as b .

We begin by considering the Stokes equations (2.1), which is a simplification of the Navier-Stokes equations neglecting inertia, resulting in a balance between the divergence of the Cauchy stress tensor, $\boldsymbol{\sigma}$ and a body force \mathbf{f} ,

$$\nabla \cdot \boldsymbol{\sigma} + \rho \mathbf{f} = 0. \quad (2.1)$$

We take the standard decomposition of the Cauchy stress tensor, $\sigma_{ij} = -p\delta_{ij} + \tau_{ij}$, where p is the pressure and $\tau_{ij} = 2\mu\dot{\epsilon}_{ij}$ are the deviatoric stresses, which are equal to twice the product of viscosity μ with the strain rate $\dot{\epsilon}_{ij}$. Strain rate is defined as $\dot{\epsilon}_{ij} = \frac{1}{2}(\partial_i u_j + \partial_j u_i)$. In a vertical plane, (x, z) , the 2-D equations can be expressed in component form as:

$$\mathbf{x}: -\partial_x p + \partial_x \tau_{xx} + \partial_z \tau_{xz} = 0 \quad (2.2a)$$

$$\mathbf{z}: \partial_x \tau_{xz} - \partial_z p + \partial_z \tau_{zz} = \rho g, \quad (2.2b)$$

where the body force, \mathbf{f} (2.1), is the vertical force of gravity, g , and ρ is ice density. To predict the ice sheet flow, we also need the mass conservation equation and additional boundary conditions. Considering ice sheet as incompressible flow with constant density, the mass conservation equation is reduced to the continuity equation, which reads

$$\partial_x u + \partial_z w = 0. \quad (2.3)$$

Neglecting the atmospheric pressure which is isotropically exerted on the ice sheet, the top surface of ice sheet experiences no extra stress, giving the dynamic boundary condition at the ice surface, $z = h$:

$$\boldsymbol{\sigma} \cdot \hat{\mathbf{n}}|_{z=h} = 0, \quad (2.4)$$

where $\hat{\mathbf{n}}$ is the unit normal vector pointing outward from the surface. We define the ice surface to be $z = h(x, y)$. Then, by introducing $f = z - h(x, y)$, the outward normal unit vector $\hat{\mathbf{n}}$ can be expressed using differential geometry as

$$\hat{\mathbf{n}} = \frac{\nabla f}{|\nabla f|} = \frac{(-\partial_x h, 1)}{\sqrt{(\partial_x h)^2 + 1}}. \quad (2.5)$$

Using the standard Cauchy stress tensor decomposition and substituting (2.5) into (2.4) yields, in component-form,

$$\left. \begin{array}{l} \mathbf{x}: p|_h \partial_x h - \tau_{xx}|_h \partial_x h + \tau_{xz}|_h = 0 \\ \mathbf{z}: -\tau_{xz}|_h \partial_x h - p|_h + \tau_{zz}|_h = 0 \end{array} \right\} \text{at } z = h. \quad (2.6)$$

In this study, we consider the bed underneath the ice sheet as a flat horizontal surface, namely a constant b . Then the boundary conditions at the bottom surface, $z = b$ then become

$$w = 0 \text{ (no penetration)} \quad \text{and} \quad \left. \begin{array}{l} \partial_z u = 0 \text{ (no stress)} \\ u = 0 \text{ (no slip)} \end{array} \right\} \text{in free-slip region} \quad \left. \begin{array}{l} \\ \\ \end{array} \right\} \text{at } z = b. \quad (2.7a)$$

2.2. Non-dimensionalization and scaling analysis

To non-dimensionalize the system, we introduce the following dimensionless variables:

$$(\tilde{x}, \tilde{z}) = \left(\frac{x}{[x]}, \frac{z}{[z]} \right), \quad (\tilde{u}, \tilde{w}) = \left(\frac{u}{[u]}, \frac{w}{[w]} \right), \quad (2.8a)$$

$$\tilde{\mu} = \frac{\mu}{[\mu]}, \quad \tilde{p} = \frac{p}{[p]}, \quad \tilde{\tau}_{ij} = \frac{\tau_{ij}}{[\tau_{ij}]}, \quad (2.8b)$$

which are denoted by the same symbol with tilde. The bracket ‘[.]’ indicates the characteristic dimensional scale of each variable. Here, we note that, for our case of a Newtonian fluid, the viscosity μ is constant over the domain. Thus, the dimensionless viscosity is set to be $\tilde{\mu} = 1$, which is applied automatically in the rest of the derivation unless specifically noted otherwise.

Because the goal of this study is to quantify the stress perturbation due to the presence of the slippery patch, our analysis will focus on the local flow pattern near that patch, namely in the domain as shown in figure 1. Within that domain, a good selection of vertical length scale is:

$$[z] \equiv h_0 \quad (2.9)$$

where h_0 is the ice thickness at the center of the slippery patch, $x = 0$. Due to the slender-body shape, the ice sheet has a small surface slope. Considering the finite length ℓ of the slippery patch, the slope of the ice surface above the patch can be further considered as a constant within the domain of interest. Here, we consider the case where the ice thickness decreases along the positive x -direction, which indicates the ice flows from left to right (figure 1). The surface slope above the slippery patch can then be written as

$$\frac{dh(x)}{dx} = -\epsilon \quad \text{for } -\frac{\ell}{2} \leq x \leq \frac{\ell}{2}, \quad (2.10)$$

where $\epsilon \ll 1$ is a small constant parameter. Then, the horizontal length scale $[x]$ of the flow can be defined as

$$[x] = \frac{[z]}{\epsilon} = \frac{h_0}{\epsilon}. \quad (2.11)$$

Taking the definition of deviatoric stress and strain rate as $\tau_{ij} = 2\mu\dot{\epsilon}_{ij}$ and $\dot{\epsilon}_{ij} = \frac{1}{2}(\partial_i u_j + \partial_j u_i)$, respectively, the deviatoric stress scales are written as

$$[\tau_{xz}] = [\mu][\dot{\epsilon}_{xz}] = \frac{[\mu][u]}{[z]}, \quad (2.12a)$$

$$\text{and } [\tau_{xx}] = [\tau_{zz}] = 2\frac{[\mu][u]}{[x]} = 2\epsilon[\tau_{xz}]. \quad (2.12b)$$

We note that the relation $[\tau_{xx}] = [\tau_{zz}]$ in (2.12b) comes from the fact that $\tau_{zz} = -\tau_{xx}$ as the deviatoric stress is trace-free. It can also be derived from the continuity equation. Substitution of the dimensionless variables (2.8) and the scaling relations (2.12) into the Stokes momentum equations (2.2) gives:

$$\mathbf{x}: -\frac{[p][z]}{[\mu][u]}\epsilon\partial_{\tilde{x}}\tilde{p} + 2\epsilon^2\partial_{\tilde{x}}\tilde{\tau}_{\tilde{x}\tilde{x}} + \partial_{\tilde{z}}\tilde{\tau}_{\tilde{x}\tilde{z}} = 0 \quad (2.13a)$$

$$\mathbf{z}: \epsilon\partial_{\tilde{x}}\tilde{\tau}_{\tilde{x}\tilde{z}} - \frac{[p][z]}{[\mu][u]}\partial_{\tilde{z}}\tilde{p} + 2\epsilon\partial_{\tilde{z}}\tilde{\tau}_{\tilde{z}\tilde{z}} = \frac{\rho g [z]^2}{[\mu][u]}. \quad (2.13b)$$

In the vertical direction (2.13b), the pressure gradient must balance the gravity term to

leading order. Thus, the pressure scale can be determined by

$$[p] = \rho g [z] = \rho g h_0. \quad (2.14)$$

Because ice flows as a viscous gravity current, for which gravity is the only driving force, its velocity scale should be determined by gravity, as well as the viscosity scale, which describes the resistance of ice sheet to the motion in response to gravity. However, for a slender-body ice sheet, its velocity scales are distinct between the no-slip region and free-slip patch. In the no-slip region, the vertical shear stress $\tilde{\tau}_{\tilde{x}\tilde{z}}$ is the dominant resistive force balancing the gravitational pressure. Thus, the shear-stress gradient term $\partial_{\tilde{z}}\tilde{\tau}_{\tilde{x}\tilde{z}}$ in the horizontal Stokes equation (2.13a) should balance the pressure gradient to leading order. This gives the expression of the horizontal velocity scale as:

$$\frac{[p][z]}{[\mu][u]} \epsilon \sim 1 \quad \Longrightarrow \quad [u] = \frac{\rho g h_0^2}{[\mu]} \epsilon, \quad (2.15)$$

where the pressure scale expression (2.14) is used.

In contrast, in the free-slip patch, due to the absence of shear stresses at the both top and bottom surfaces, the ice sheet there should experience no vertical shear stress. Namely, the shear-stress gradient term $\partial_{\tilde{z}}\tilde{\tau}_{\tilde{x}\tilde{z}}$ in (2.13a) becomes negligible. Then, the dominant resistance force becomes the horizontal extensional stress $\tilde{\tau}_{\tilde{x}\tilde{x}}$, and its gradient term $\partial_{\tilde{x}}\tilde{\tau}_{\tilde{x}\tilde{x}}$ in (2.13a) should balance the pressure gradient to leading order, which leads to

$$\frac{[p][z]}{[\mu][u]} \epsilon \sim \epsilon^2 \quad \Longrightarrow \quad [u] = \frac{\rho g h_0^2}{[\mu]} \epsilon^{-1}. \quad (2.16)$$

Comparing (2.15) and (2.16) and considering $\epsilon \ll 1$, we show that the velocity scale in the free-slip patch is $O(\epsilon^{-2})$ larger than that in the no-slip regions, which is simply because the predominant shear stress $\tilde{\tau}_{\tilde{x}\tilde{z}}$ in the no-slip region is $O(\epsilon^{-2})$ larger than the predominant extensional stress $\tilde{\tau}_{\tilde{x}\tilde{x}}$ in the free-slip patch, as shown in (2.13a).

To mathematically reconcile the horizontal velocity scale in both no-slip and free-slip regions, we introduce a new dimensionless parameter, δ , by which the horizontal velocity scale can be written in a succinct way as:

$$[u] = \frac{\rho g h_0^2}{[\mu] \delta} \epsilon \quad \text{with} \quad \delta = \begin{cases} \epsilon^2 & \text{in free-slip patch} \\ 1 & \text{in no-slip regions.} \end{cases} \quad (2.17)$$

With this horizontal velocity scale, the vertical velocity scale can be determined from the continuity equation (2.3). Substitution of the dimensionless velocity (2.8) into the continuity equation (2.3), the vertical velocity scale can be determined by:

$$\frac{[u]}{[x]} \partial_{\tilde{x}} \tilde{u} + \frac{[w]}{[z]} \partial_{\tilde{z}} \tilde{w} = 0 \quad \Longrightarrow \quad [w] = \epsilon [u] = \frac{\rho g h_0^2}{[\mu]} \delta. \quad (2.18)$$

Then, substitution of the pressure scale (2.14) and velocity scale (2.17) into the Stokes equations (2.13) gives the dimensionless Stokes equations:

$$\mathbf{x}: \quad -\delta \partial_{\tilde{x}} \tilde{p} + 2\epsilon^2 \partial_{\tilde{x}} \tilde{\tau}_{\tilde{x}\tilde{x}} + \partial_{\tilde{z}} \tilde{\tau}_{\tilde{x}\tilde{z}} = 0 \quad (2.19a)$$

$$\mathbf{z}: \quad -\delta (\partial_{\tilde{z}} \tilde{p} + 1) + 2\epsilon^2 \partial_{\tilde{z}} \tilde{\tau}_{\tilde{z}\tilde{z}} + \epsilon^2 \partial_{\tilde{x}} \tilde{\tau}_{\tilde{x}\tilde{z}} = 0. \quad (2.19b)$$

Similarly, substitution of all the dimensionless variables (2.8) and their scale relations (2.12), (2.17) into the dynamic surface boundary condition (2.6) gives its non-dimensional version

$$\left. \begin{aligned} \mathbf{x}: & \quad -\delta \partial_{\tilde{x}} \tilde{p} + 2\epsilon^2 \partial_{\tilde{x}} \tilde{\tau}_{\tilde{x}\tilde{x}} + \partial_{\tilde{z}} \tilde{\tau}_{\tilde{x}\tilde{z}} = 0 \\ \mathbf{z}: & \quad -\delta (\partial_{\tilde{z}} \tilde{p} + 1) + 2\epsilon^2 \partial_{\tilde{z}} \tilde{\tau}_{\tilde{z}\tilde{z}} + \epsilon^2 \partial_{\tilde{x}} \tilde{\tau}_{\tilde{x}\tilde{z}} = 0 \end{aligned} \right\} \text{on } \tilde{z} = \tilde{h}, \quad (2.20)$$

with δ given in (2.17).

2.3. Perturbation series expansions

To derive the reduced-order model, we first introduce the perturbation series expansions for the dimensionless velocities and pressure in terms of ϵ^2 by:

$$\tilde{u} = \tilde{u}_0 + \epsilon^2 \tilde{u}_1 + O(\epsilon^4), \quad \tilde{w} = \tilde{w}_0 + \epsilon^2 \tilde{w}_1 + O(\epsilon^4), \quad (2.21a)$$

$$\tilde{\tau}_{ij} = \tilde{\tau}_{ij_0} + \epsilon^2 \tilde{\tau}_{ij_1} + O(\epsilon^4), \quad \tilde{p} = \tilde{p}_0 + \epsilon^2 \tilde{p}_1 + O(\epsilon^4), \quad (2.21b)$$

where $\tilde{\tau}_{ij}$ indicates the dimensionless deviatoric stress components, namely $\tilde{\tau}_{\tilde{x}\tilde{x}}$, $\tilde{\tau}_{\tilde{x}\tilde{z}}$, and $\tilde{\tau}_{\tilde{z}\tilde{z}}$. Given the stress scale (2.12) and the velocity scales (2.17) and (2.18), the relation of the dimensionless shear stress component $\tilde{\tau}_{\tilde{x}\tilde{z}}$ with the velocity (\tilde{u} , \tilde{w}) gives

$$[\tau_{xz}] \tilde{\tau}_{\tilde{x}\tilde{z}} = \frac{[\mu][u]}{[z]} \partial_{\tilde{z}} \tilde{u} + \frac{[\mu][w]}{[x]} \partial_{\tilde{x}} \tilde{w} \implies \tilde{\tau}_{\tilde{x}\tilde{z}} = \partial_{\tilde{z}} \tilde{u} + \epsilon^2 \partial_{\tilde{x}} \tilde{w}, \quad (2.22)$$

while the relation of dimensionless deviatoric normal stress components ($\tilde{\tau}_{\tilde{x}\tilde{x}}$, $\tilde{\tau}_{\tilde{z}\tilde{z}}$) gives

$$-[\tau_{zz}] \tilde{\tau}_{\tilde{z}\tilde{z}} = [\tau_{xx}] \tilde{\tau}_{\tilde{x}\tilde{x}} = 2 \frac{[\mu][u]}{[x]} (\partial_{\tilde{x}} \tilde{u}) \implies -\tilde{\tau}_{\tilde{z}\tilde{z}} = \tilde{\tau}_{\tilde{x}\tilde{x}} = \partial_{\tilde{x}} \tilde{u}. \quad (2.23)$$

Substitution of the perturbation expansion of velocity (2.21a) into (2.22) and (2.23) gives the relation of the stress expansion term with respect to the velocity expansion terms as

$$\tilde{\tau}_{\tilde{x}\tilde{z}_0} = \partial_{\tilde{z}} \tilde{u}_0, \quad \tilde{\tau}_{\tilde{x}\tilde{z}_1} = \partial_{\tilde{z}} \tilde{u}_1 + \partial_{\tilde{x}} \tilde{w}_0, \quad (2.24a)$$

$$\tilde{\tau}_{\tilde{x}\tilde{x}_0} = \partial_{\tilde{x}} \tilde{u}_0, \quad \tilde{\tau}_{\tilde{x}\tilde{x}_1} = \partial_{\tilde{x}} \tilde{u}_1, \quad (2.24b)$$

$$\tilde{\tau}_{\tilde{z}\tilde{z}_0} = \partial_{\tilde{z}} \tilde{w}_0 = -\partial_{\tilde{x}} \tilde{u}_0, \quad \tilde{\tau}_{\tilde{z}\tilde{z}_1} = \partial_{\tilde{z}} \tilde{w}_1 = -\partial_{\tilde{x}} \tilde{u}_1, \quad (2.24c)$$

where the last equality in (2.24c) uses the continuity equation (2.3). In the following sections, we separate the derivations for the reduced-order model in the no-slip and free-slip zones. Because the remainder of the derivation are based on dimensionless variables, we drop tildes for the non-dimensional variables unless explicitly stated otherwise. We will begin with the free-slip patch interior.

2.4. Depth-averaged model for free-slip patch

In regions with a free-slip basal boundary condition, ice flow is characterized by a dominant balance between the gravitational pressure and horizontal extensional stress, where the velocity scale is expressed by (2.17) with $\delta = \epsilon^2$. Upon perturbation series expansion (2.21b), we obtain the extension-dominated truncated Stokes equations with accuracy up to $O(\epsilon^4)$:

$$\mathbf{x}: \partial_z \tau_{xz_0} + \epsilon^2 [-\partial_x p_0 + 2\partial_x \tau_{xx_0} + \partial_z \tau_{xz_1}] = 0, \quad (2.25a)$$

$$\mathbf{z}: -(\partial_z p_0 + 1) + 2\partial_z \tau_{zz_0} + \partial_x \tau_{xz_0} + \epsilon^2 [-\partial_z p_1 + 2\partial_x \tau_{zz_1} + \partial_x \tau_{xz_1}] = 0, \quad (2.25b)$$

with the associated truncated boundary conditions at the free surface

$$\mathbf{x}: \tau_{xz_0} + \epsilon^2 [\tau_{xz_1} + p_0 h_x - 2\tau_{xx_0} h_x] = 0, \quad (2.26a)$$

$$\mathbf{z}: -\tau_{xz_0} h_x - p_0 + 2\tau_{zz_0} + \epsilon^2 [-\tau_{xz_1} h_x - p_1 + 2\tau_{zz_1}] = 0. \quad (2.26b)$$

Taking the leading-order terms $O(1)$ in the system yields:

$$\tau_{xz_0} = \partial_z u_0 = 0, \quad (2.27a)$$

$$p_0 = (h - z) + 2\tau_{zz_0}, \quad (2.27b)$$

which indicates the ice sheet behaves as solid ice at the leading order, but does not provide any information about the velocity field. Thus, we turn to the $O(\epsilon^2)$ terms in the system.

Stokes equations, $O(\epsilon^2)$:

$$\mathbf{x}: -\partial_x p_0 + 2\partial_x \tau_{xx_0} + \partial_z \tau_{xz_1} = 0, \quad (2.28a)$$

$$\mathbf{z}: -\partial_z p_1 + 2\partial_x \tau_{zz_1} + \partial_x \tau_{xz_1} = 0, \quad (2.28b)$$

Free surface conditions, $O(\epsilon^2)$:

$$\mathbf{x}: \tau_{xz_1}|_h + p_0|_h h_x - 2\tau_{xx_0}|_h h_x = 0, \quad (2.29a)$$

$$\mathbf{z}: -\tau_{xz_1}|_h h_x - p_1|_h + 2\tau_{zz_1}|_h = 0. \quad (2.29b)$$

Taking the integral of the $O(\epsilon^2)$ x -direction Stokes equation (2.28a) along the z -direction and applying the free surface conditions (2.29), we have:

$$\begin{aligned} & -\partial_x \int_b^h p_0 dz + 2\partial_x \int_b^h \tau_{xx_0} dz + \dots \\ & \underbrace{\dots + 2\tau_{xx_0}|_b b_x + \tau_{xz_1}|_h + p_0|_h h_x - 2\tau_{xx_0}|_h h_x}_{=0 \text{ (2.29a)}} - \underbrace{\tau_{xz_1}|_b}_{\tau_{xz}|_b = 0 \text{ (2.7)}} = 0 \end{aligned} \quad (2.30a)$$

$$\Rightarrow -\partial_x \int_b^h p_0 dz + 2\partial_x \int_b^h \tau_{xx_0} dz = 0, \quad (2.30b)$$

where we have recognized a few terms drop out due to the flat bed ($b_x = 0$), the free surface (2.29a), and the shear-free basal boundary condition. Substitution of the leading-order pressure, p_0 (2.27b) yields

$$-hh_x + 4\partial_x \int_b^h \partial_x u_0 dz = 0, \quad (2.31)$$

where stress expansion terms are replaced by the velocity expansion terms based on (2.24). The equation now becomes an ordinary differential equation of the horizontal velocity u with respect to x . Applying Leibniz rule to the integral in (2.31), we have

$$-hh_x + 4\partial_x \left[\partial_x \int_b^h u_0 dz - u_0|_h h_x + \underbrace{u_0|_b b_x}_{b_x = 0} \right] = 0. \quad (2.32)$$

We recall that the leading-order horizontal velocity is depth-independent (2.27a), which gives $u_0(z) = u_0|_h = \bar{u}_0$, where \bar{u}_0 is defined as the depth-averaged horizontal velocity. Substitution of the relation into (2.32) gives the reduced-order 1D governing equation in the free-slip region:

$$-hh_x + 4(\bar{u}_0)_x h = 0 \quad (2.33)$$

We note that a derivation of a similar model may be found in MacAyeal (1989), for the case of grounded ice sliding over highly-deformable sediment, though here we consider zero basal shear stress. This model is also similar to that which describes the extensional flow of ice shelves, but without buoyancy. We now turn to the no-slip regions surrounding the patch.

2.5. Depth-averaged model for no-slip regions

In the no-slip regions, the gravitational pressure is mainly balanced by the the vertical shear stress, which leads to velocity scale (2.17) with $\delta = 1$, much smaller than that in the free-slip region. With a substitution of the expansion (2.24), we obtain the shear-dominated truncated

Stokes equations, accurate up to $O(\epsilon^4)$:

$$\mathbf{x}: -\partial_x(p_0 + \epsilon^2 p_1) + 2\epsilon^2 \partial_x \tau_{xx_0} + \partial_z(\tau_{xz_0} + \epsilon^2 \tau_{xz_1}) = 0, \quad (2.34a)$$

$$\mathbf{z}: -\left(\partial_z(p_0 + \epsilon^2 p_1) + 1\right) + 2\epsilon^2 \partial_z \tau_{zz_0} + \epsilon^2 \partial_x \tau_{xz_0} = 0, \quad (2.34b)$$

with the associated dynamic boundary condition at the free surface

$$\mathbf{x}: (p_0|_h + \epsilon^2 p_1|_h)h_x - 2\epsilon^2 \tau_{xx_0}|_h h_x + (\tau_{xz_0}|_h + \epsilon^2 \tau_{xz_1}|_h) = 0, \quad (2.35a)$$

$$\mathbf{z}: -\epsilon^2 \tau_{xz_0}|_h h_x - (p_0|_h + \epsilon^2 p_1|_h) + 2\epsilon^2 \tau_{zz_0}|_h = 0. \quad (2.35b)$$

Taking the leading-order $O(1)$ terms in the z -direction Stokes equation (2.34b) and z -direction free surface condition (2.35b) gives

$$p_0(z) = (h - z). \quad (2.36)$$

We substitute (2.36) and the expression of stress with velocity (2.24) into (2.34a). By taking its leading-order terms, we have

$$u_0(x, z) = -h_x \left(hz - \frac{z^2}{2} \right). \quad (2.37)$$

Then, the depth-averaged leading-order horizontal velocity is

$$\bar{u}_0(x) = \frac{1}{h} \int_{b=0}^h u_0(x, z) dz = -\frac{1}{3} h_x h^2. \quad (2.38)$$

In addition, the leading-order horizontal velocity at the free surface ($z = h$) simply reads

$$u_0|_h = u_0(x, h) = -\frac{1}{2} h_x h^2, \quad (2.39)$$

which can also be expressed in terms of the depth-averaged velocity by:

$$u_0|_h = u_0(x, h) = \frac{3}{2} \bar{u}_0(x). \quad (2.40)$$

Now, we consider the system involving the second-order terms, $O(\epsilon^2)$ (2.34)-(2.35). Taking the vertical integral of the z -Stokes equation (2.34b) and using the free-surface boundary conditions (2.35b), we have

$$(p_0 + \epsilon^2 p_1) = (h - z) + 2\epsilon^2 \tau_{zz_0} - \epsilon^2 \partial_x \int_z^h \tau_{xz_0} dz = 0. \quad (2.41)$$

Substitution of the stress relation with velocity (2.24) gives

$$(p_0 + \epsilon^2 p_1) = (h - z) - \epsilon^2 [\partial_x u_0(x, h) + \partial_x u_0(x, z)]. \quad (2.42)$$

Similarly, taking the vertical integral of the x -equation (2.34a) and using the surface boundary condition (2.35a), we have

$$-\partial_x \int_b^h (p_0 + \epsilon^2 p_1) dz - \tau_{xz_0}|_b + 2\epsilon^2 \partial_x \int_b^h \tau_{xx_0} dz - \epsilon^2 \tau_{xz_1}|_b - \underbrace{(p_0 + \epsilon^2 p_1)|_b}_{b_x = 0} b_x = 0, \quad (2.43a)$$

where the last term is eliminated due to the flat bed. Substitution of stress relation with

velocity (2.24), as well as substitution of the pressure (2.41), yields

$$-\partial_x \int_b^h (h-z) dz + \epsilon^2 \partial_x \left[\partial_x \int_b^h u_0|_h dz + \partial_x \int_b^h u_0|_z dz - 2u_0|_h h_x \right] + \dots \\ \dots - \tau_{xz_0}|_b - \epsilon^2 \tau_{xz_1}|_b + 2\epsilon^2 \partial_x \left(\partial_x \int_b^h u_0 dz - u_0|_h h_x \right) = 0. \quad (2.44)$$

By definition, we have

$$\int_b^h u_0 dz = h\bar{u}_0 \quad \text{and} \quad \int_b^h u_0|_h dz = hu_0|_h, \quad (2.45)$$

where \bar{u}_0 is the depth-averaged leading-order horizontal velocity. Substitution of (2.45) into (2.44) gives

$$-hh_x - \tau_{xz_0}|_b - \epsilon^2 \tau_{xz_1}|_b + \epsilon^2 \partial_{xx}(hu_0|_h) + 3\epsilon^2 \partial_{xx}(h\bar{u}_0) - 4\epsilon^2 \partial_x(u_0|_h h_x) = 0 \quad (2.46)$$

Recalling the relation (2.40) between leading-order surface velocity $u_0|_h$ and depth-averaged velocity \bar{u}_0 , the equation can be further simplified as

$$-hh_x - \tau_{xz_0}|_b - \epsilon^2 \tau_{xz_1}|_b + \frac{3}{2}\epsilon^2 [3(\bar{u}_0 h)_x - (\bar{u}_0 h_x)_x] = 0. \quad (2.47)$$

Using (2.24), (2.37) and (2.38), the leading-order shear stress at the bottom $\tau_{xz_0}|_b$ can also be expressed in terms of the depth-averaged velocity by

$$\tau_{xz_0}|_b = \partial_z u_0(x, z)|_{z=0} = -hh_x = 3\frac{\bar{u}_0}{h}. \quad (2.48a)$$

For the second-order shear stress term, τ_{xz_1} , we may use (2.24) to write $\tau_{xz_1} = \partial_z u_1 + \partial_x w_0$ and note that at the bed, which in our case is flat, we have no vertical velocity, meaning that $w_0 = \partial_x w_0 = 0$, leaving us with $\tau_{xz_1}|_b = \partial_z u_1|_b$. Now we can write our overall depth-averaged equation for the no-slip region, which is accurate up to $O(\epsilon^4)$, as

$$-hh_x - 3\frac{\bar{u}_0}{h} - \epsilon^2 \partial_z u_1|_b + \frac{3}{2}\epsilon^2 [3(\bar{u}_0 h)_x - (\bar{u}_0 h_x)_x] = 0. \quad (2.49)$$

2.6. Summary of the reduced-order model

In summary, the governing equations derived above represent a 1D reduced-order model which we can evaluate in the no-slip regions (upstream and downstream from the patch) and in the free-slip regions (interior to the patch). These equations are closed by appropriate boundary conditions, which will be discussed in detail in the following section. Here, it is important to note that the velocities in the free- and no-slip regions maintain different scales, where the velocity in the free-slip region (2.16) is much faster than that in the no-slip region (2.15) due to the lack of basal resistance. To distinguish between these two scales, from now on, we denote $[u]$ as the horizontal velocity scale in the no-slip region only, and redefine the horizontal velocity scale within the free-slip patch region as $[v]$. Namely, referring to (2.17), we separate the relations for the free-slip and no-slip velocity scales as

$$[u] = \frac{\rho g h_0^2}{[\mu]} \epsilon \quad \text{and} \quad [v] = \frac{\rho g h_0^2}{[\mu]} \epsilon^{-1} \quad (2.50a)$$

$$\Rightarrow [u] = \epsilon^2 [v]. \quad (2.50b)$$

With these distinct scales in mind, we summarize below the equations governing our system.

Free-slip governing equation:

$$\underbrace{-hh_x}_{\text{pressure}} + 4\underbrace{(\bar{v}_{0_x}h)_x}_{\text{extension}} = 0, \quad (2.51)$$

No-slip governing equation:

$$\underbrace{-hh_x}_{\text{pressure}} - \underbrace{3\frac{\bar{u}_0}{h}}_{\text{shear}} - \underbrace{\epsilon^2 \partial_z u_1|_b}_{O(\epsilon^2) \text{ shear}} + \underbrace{\frac{3}{2}\epsilon^2 [3(\bar{u}_{0_x}h)_x - (\bar{u}_0h_x)_x]}_{O(\epsilon^2) \text{ extension}} = 0, \quad (2.52)$$

where v represents the dimensionless velocity non-dimensionalized by the velocity scale $[v]$ in the free-slip zone, and u is non-dimensionalized by $[u]$ in the no-slip zone. We recall that the free-slip region is governed by a balance between pressure and extensional stress (2.51), while the no-slip region is governed by a dominant balance between pressure and shear, with $O(\epsilon^2)$ contributions of extensional stress and a secondary shear term (2.52). Both the free- and the no-slip equations are accurate up to $O(\epsilon^4)$. We now turn to solving these governing equations and derive the solution that links these two regions.

3. Matched asymptotics

To quantify the stress field's response to the presence of a slippery patch, we need to connect the solution between the no-slip region with that in the free-slip patch. Considering the Newtonian flow with constant viscosity, the expression for the stress field is equivalent to that of the strain rate, save for a factor of two. Thus, we solve first for the strain rate across the slippery patch. This solution sets a boundary condition at the upstream transition point which can not be satisfied by the leading-order strain rate in the no-slip region, motivating the need to employ a boundary layer approach near to, but upstream from, the transition point. Based on matched asymptotics analysis, we construct a boundary layer solution by locally rescaling the system variables and upholding the physical transition from the no-slip (shear-dominated flow, slower velocity) region to the free-slip (extension-dominated, faster velocity) region. The result is an analytical expression that reveals a clear structure underlying the relationships between ice sheet geometry and the perturbed strain rate (stress) response.

3.1. Patch interior solution

In the free-slip region across the patch, the strain rate of the ice sheet can be solved simply by taking the integral of the equation (2.51) with respect to x , which gives

$$\bar{v}_{0_x} = \frac{h}{8} + \frac{c_1}{h}, \quad (3.1)$$

where c_1 is a constant to be determined. Recalling the slender-body shape of ice sheet (figure 1), the surface slope above the finite-length patch size can be considered as a constant in the domain of interest (2.10). In addition, because we define the thickness at the center of the slippery patch as $h(x=0) = h_0$, the surface profile above the slippery patch can then be expressed in the dimensional version as

$$h^*(x^*) \approx h_0 - \epsilon x^* \quad \text{for } -\frac{\ell}{2} \leq x^* \leq \frac{\ell}{2}, \quad (3.2)$$

recalling that ϵ is the negative of surface slope (2.10). Here on, we use (*) to denote dimensional variables. Using the vertical (2.9) and horizontal (2.11) length scales, the

dimensionless surface profile h with respect to the dimensionless spatial variables x gives:

$$h(x) = 1 - x \quad \text{for } -\frac{\lambda}{2} \leq x \leq \frac{\lambda}{2}, \quad (3.3)$$

with

$$\lambda \equiv \frac{\ell}{[x]} = \frac{\ell}{h_0} \epsilon. \quad (3.4)$$

Considering the case where the finite-length patch ℓ is larger than the ice thickness but much less than the ice sheet length scale $[x]$, namely $h_0 \ll \ell \ll [x]$, gives $\epsilon \ll \lambda \ll 1$. Substitution of (3.3) into (3.1) yields:

$$\bar{v}_{0_x} = \frac{1-x}{8} + \frac{c_1}{1-x}. \quad (3.5)$$

To determine the unknown coefficient c_1 , we note that across the upstream transition point, the ice velocity increases due to the transition from the no-slip to free-slip basal boundary, which results in extensional stresses. Inversely, across the downstream transition point (free-slip to no-slip basal boundary), compressive stresses develop. Assuming this stress pattern across the patch is symmetrical at the leading-order, which is confirmed by the simulation in the next section (see figure 4), we take the strain rate to be zero at the patch center, namely

$$\bar{v}_{0_x}(0) = \frac{1}{8} + c_1 = 0 \quad \implies \quad c_1 = -\frac{1}{8}. \quad (3.6)$$

Then, the strain rate across the patch becomes:

$$\bar{v}_{0_x}(x) = \frac{1}{8} \left(1 - x - \frac{1}{1-x} \right). \quad (3.7)$$

We further simplify the strain rate function by taking a Taylor series expansion of the strain rate and approximate the strain rate across the patch interior (accurate up to $O(x^2)$) as

$$\bar{v}_{0_x}(x) \approx \frac{1}{8}(-2x) = -\frac{1}{4}x. \quad (3.8)$$

Thus, the value of strain rate at the upstream transition point $x = -\lambda/2$ gives

$$\bar{v}_{0_x}^{(\text{up})} = \bar{v}_{0_x}|_{(x=-\lambda/2)} = \frac{\lambda}{8}. \quad (3.9)$$

The strain rate at the downstream transition point is determined following an analogous derivation but located at $x = \lambda/2$, and results in

$$\bar{v}_{0_x}^{(\text{down})} = \bar{v}_{0_x}|_{(x=\lambda/2)} = -\frac{\lambda}{8}. \quad (3.10)$$

The strain rate value at the upstream transition point (3.9) serves as the right-side boundary condition for the strain rate in the upstream no-slip system. Similarly, the strain rate value at the downstream transition point (3.10) serves as the left-side boundary condition for the strain rate in the downstream no-slip system. We focus the following derivation on the transition point at the upstream end of the patch, but will display the results for the downstream point, noting that that the derivation is analogous. Recalling the expressions of the stress scale (2.12b) with the vertical length scale (2.9) and the free-slip horizontal velocity scale $[v]$ (2.50), the dimensional stress function in the free-slip patch is derived as

$$\tau_{x^*x^*}^*(x^*) = 2\epsilon \frac{[\mu][v]}{[z]} \bar{v}_{0_x} \left(\frac{x^*}{[x]} \right) = 2\rho g h_0 \cdot \left(-\frac{x^*}{4[x]} \right) = -\frac{1}{2}\rho g \epsilon x^* \quad \text{for } -\frac{\ell}{2} \leq x^* \leq \frac{\ell}{2}. \quad (3.11)$$

Thus, the dimensional stress at the upstream (and downstream) transition point is given by

$$\tau_{x^*x^*}^{*(\text{up})} = -\tau_{x^*x^*}^{*(\text{down})} = \tau_{x^*x^*}^* \Big|_{x^*=-\frac{\ell}{2}} = \frac{1}{4} \rho g \ell \epsilon. \quad (3.12)$$

Physically, the expression (3.12) indicates that the stress magnitude at the transition point is determined by the pressure drop across the free-slip patch. As we will see in the upcoming section, this boundary condition can not be satisfied by the leading-order no-slip governing equation, leaving us with a singular perturbation problem and motivating the use of a boundary-layer approach to resolve the dynamics in the upstream no-slip region near to the transition point.

3.2. Singular perturbation in the no-slip region

To evaluate the strain rate (stress) in the no-slip region near to the patch onset, we return to the no-slip governing equation (2.52). In the limit where $\epsilon = 0$, we recover the shear-dominated velocity solution from (2.38) which can be differentiated to yield the strain rate:

$$\bar{u}_{0,x} = -\frac{1}{3} h_{xx} h^2 - \frac{2}{3} h h_x^2. \quad (3.13)$$

Considering the slender-body shape of the ice sheet, the ice surface in the no-slip zone near the finite-length slippery patch should have approximately the same constant slope, ϵ , as that in the free-slip zone. Thus, the surface profile can be expressed the same as (3.3), namely $h \approx 1 - x$. Substitution of (3.3) into (3.13) gives

$$\bar{u}_{0,x} \approx -\frac{2}{3} (1 - x). \quad (3.14)$$

Then, the strain rate in the no-slip zone close to the transition point $x = -\lambda/2$ gives

$$\bar{u}_{0,x}^{(\text{up})} = \bar{u}_{0,x} \Big|_{x=-\frac{\lambda}{2}} = -\frac{2+\lambda}{3} \sim O(1). \quad (3.15)$$

Recalling the expressions of the stress scale (2.12b) with the vertical length scale (2.9) and the no-slip horizontal velocity scale $[u]$ (2.50), the dimensional stress in the no-slip zone near the transition point is derived as

$$\tau_{x^*x^*}^{*(\text{up})'} = 2\epsilon \frac{[\mu][u]}{[z]} \bar{u}_{0,x}^{(\text{up})} = 2\rho g h_0 \epsilon^2 \cdot O(1), \quad (3.16)$$

which is much smaller than the stress (3.12) derived from the free-slip patch at the upstream transition point.

To reconcile the mismatch of the stress between the no-slip and free-slip zone at the interface of the transition point, we recall that the reduced-order model (2.52) in the no-slip region is in fact a singular perturbed equation. When close to the transition point, the $O(\epsilon^2)$ terms, standing for extensional stress, in equation (2.52) must become dominant, resulting in the existence of a transition region around the interface between the no-slip and free-slip zone, known as a boundary layer. The model in the boundary layer can be developed by employing matched asymptotic analysis as conducted in the next section.

3.3. Upstream boundary layer

To reconcile the mismatch of stresses at the upstream transition point as discussed above, we introduce a boundary-layer region in the no-slip zone close to the transition point. We note here that a boundary layer similar in structure will develop near the downstream transition point as well. In this section, we will first focus on the full derivation of the boundary layer

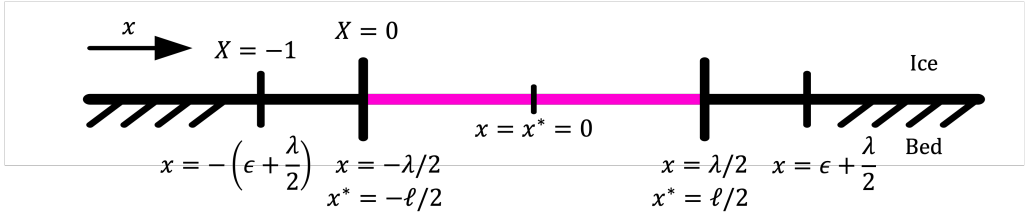


Figure 2: Along-flow coordinates (dimensionless) showing both the outer variables x for the far-field no-slip (black) and free-slip (pink) regions and the inner variables X for the boundary layer region (displayed above the line).

at the upstream transition point. A similar derivation at the downstream point is summarized in the next section.

To demonstrate that the $O(\epsilon^2)$ extensional-stress term in (2.52) becomes dominant in the boundary layer, we introduce a new local coordinate (X, Z) within the boundary-layer region, which we will also call the ‘inner’ region, as opposed to the ‘outer’ regions, far from the transition points. Because the ice sheet within the boundary layer has the same thickness scale with the outer region, we define

$$Z = z \quad \text{and} \quad H(X) = h(x), \quad (3.17)$$

where (x, z) are the dimensionless coordinates for the outer regions. For convenience, we define the origin of the local coordinates of the boundary-layer region at the upstream transition point. However, the length scale of the boundary layer unknown at present, and will be determined later. Thus, we define the new horizontal local coordinate X to be

$$\epsilon^\beta X = x + \lambda/2, \quad (3.18)$$

where β is an unknown coefficient that represents the length scale of the boundary layer with respect to the outer region. In addition, the velocity scale in the boundary layer is also different from that in the outer region and remains unknown so far. We define the new local velocity by

$$\epsilon^\gamma U(X) = \bar{u}_0(x), \quad (3.19a)$$

$$\epsilon^\gamma U_1(X, Z)|_b = u_1(x, z)|_b, \quad (3.19b)$$

where γ is another unknown coefficient representing the local velocity scale in the boundary layer region with respect to that in the outer region. Substituting these new variables (3.17)-(3.19) into our no-slip model (2.52) gives

$$\underbrace{-\epsilon^{-\beta} H H_X}_{\text{pressure}} - \underbrace{3\epsilon^\gamma \frac{U}{H}}_{\text{shear}} - \underbrace{\epsilon^{2+\gamma} \partial_Z U_1|_b}_{\text{shear correction}} + \underbrace{\frac{3}{2}\epsilon^{2+\gamma-2\beta} [3(U_X H)_X - (U H_X)_X]}_{\text{extension}} = 0. \quad (3.20)$$

We recall the balance of the strain rate (stress) in the free-slip patch, which is dominated by extensional stresses (2.51) and in the no-slip region (2.52), which is dominated by shear stresses. The boundary-layer region between the two should thus behave as a transitional zone where the shear and extensional stresses are balanced at leading-order. Equating the ϵ exponents of the shear and extension terms, $\gamma = 2 + \gamma - 2\beta$ sets $\beta = 1$. Additionally, we note that gravity pressure, as the only driving force in the system, must be another leading-order term that balance both the shear and extensional stress, giving $-\beta = \gamma$. We thus have

$$\gamma = -\beta = -1. \quad (3.21)$$

Substitution of (3.21) into (3.18) gives

$$\epsilon X = x + \lambda/2. \quad (3.22)$$

This indicates that the length scale of the boundary-layer region, $[x_{\text{bl}}]$, is given by

$$[x_{\text{bl}}] = \epsilon[x] = \frac{h_0}{[x]}[x] = h_0, \quad (3.23)$$

which is equal to the vertical length scale h_0 . Then, substitution of (3.21) into (3.19) gives

$$\epsilon^{-1}U(X) = \bar{u}_0(x). \quad (3.24)$$

This indicates that the velocity scale in the boundary-layer regions, $[u_{\text{bl}}]$, reads

$$[u_{\text{bl}}] = \epsilon^{-1}[u] = \frac{\rho g h_0^2}{[\mu]}, \quad (3.25)$$

where the last equality uses the expression of horizontal velocity scale $[u]$ (2.50) from the no-slip outer zone. Here, we find that the horizontal velocity scale $[u_{\text{bl}}]$ in the boundary-layer region is just between the velocity scale in the no-slip outer zone $[u]$ and free-slip outer zone $[v]$,

$$[u_{\text{bl}}] = \epsilon^{-1}[u] = \epsilon[v], \quad (3.26)$$

which confirms that the boundary-layer region behaves as a transitional zone that links the gap of both the velocity and stress scales in the no-slip and free-slip zone around the transition point. Finally, we substitute (3.21) into (3.20) and take the leading-order $O(1)$ terms, giving the normalized governing equation in the boundary-layer region:

$$-HH_X - 3\frac{U}{H} + \frac{3}{2}[3(U_X H)_X - (U H_X)_X] = 0. \quad (3.27)$$

Recalling the slender-body shape of the ice sheet, the surface slope in the boundary layer region next to the finite-length slippery patch can also be considered as constant, so that the surface profile remains expressed by (3.3). Using (3.19) and (3.22), the surface profile can then be expressed in terms of the local variables in the boundary-layer region by:

$$h(x) = 1 - x \quad \implies \quad H(X) = 1 - \epsilon X + \frac{\lambda}{2} \equiv H^- - \epsilon X, \quad (3.28)$$

where, for simplicity, we define $H^- = 1 + \lambda/2$, which indicates the dimensionless ice thickness at the upstream transition point. Then, substitution of (3.28) into (3.27) gives

$$U_{XX}H^- - \epsilon U_{XX}X - \frac{2}{3}\epsilon U_X - \frac{2U}{3H^-} \left(1 + \epsilon \frac{X}{H^-}\right) + \frac{2}{9}\epsilon H^- + O(\epsilon^2) = 0. \quad (3.29)$$

By taking the leading-order $O(1)$ terms only, the governing equation in the boundary-layer regions simplifies to

$$\underbrace{U_{XX}H^-}_{\text{extension}} - \underbrace{\frac{2U}{3H^-}}_{\text{shear}} = 0, \quad (3.30)$$

where the dominant balance occurs between the shear and extensional stresses. Because equation (3.30) is a second-order ordinary differential equation, its solution requires two boundary conditions. Considering that the boundary layer region is the transition zone that connects the no-slip and free-slip regions around the transition point, the two boundary conditions for the equation (3.30) should be the matching conditions that connect either

the velocity or the stress in the no-slip and free-slip zones. Recalling from (3.25) that the horizontal velocity scale $[u]$ in the no-slip region is one order of magnitude $O(\epsilon)$ less than the scale $[u_{bl}]$ in the boundary-layer region (3.26), this provides the first matching condition:

$$\lim_{X \rightarrow -\infty} U \sim O(\epsilon) \quad \implies \quad \lim_{X \rightarrow -\infty} U \approx 0. \quad (3.31)$$

Then, the second matching condition should enforce that the strain rate in the boundary layer region and the free-slip region should match at the transition point, $X = 0$. We recall that the strain rate in the free-slip region at the transition point is derived in (3.9). Considering the relation of the local variables in the boundary-layer region to that in the outer regions, the second boundary condition of (3.30) can be expressed (via a change of variables) by

$$U_X(X = 0) = \frac{U}{v_0} \cdot \frac{\partial x}{\partial X} \cdot \bar{v}_{0_x}^{(up)} = \frac{1}{\epsilon} \cdot \epsilon \cdot \frac{\lambda}{8} = \frac{\lambda}{8}. \quad (3.32)$$

Combining equation (3.30) with the two boundary conditions (3.31) and (3.32), the strain rate (and therefore also stress) within the boundary-layer region near the upstream transition point can be derived as:

$$U_X = \frac{\lambda}{8} \exp \left[\sqrt{\frac{2}{3}} \frac{X}{H^-} \right], \quad (3.33)$$

which clearly shows that the depth-averaged strain rate (stress) exponentially increases when approaching the onset of the slippery patch. Recalling the horizontal length scale $[x_{bl}]$ (3.23) and velocity scale $[u_{bl}]$ (3.25), and the expression of λ (3.4), the dimensional strain rate $u_{x^*}^*$ with respect to the dimensional coordinate x^* in the upstream boundary layer is written as:

$$\bar{u}_{0_{x^*}}^* = \frac{[u_{bl}]}{[x_{bl}]} U_X = \frac{\rho g \ell \epsilon}{8[\mu]} \exp \left[\frac{\sqrt{2/3}}{h^{*-}} \left(x^* + \frac{\ell}{2} \right) \right], \quad (3.34a)$$

where $h^{*-} = H^- h_0 = h_0 + \ell \epsilon / 2$ is the dimensional ice thickness at the upstream transition point. Then, the dimensional stress in the boundary-layer region at the upstream transition point is

$$\tau_{x^* x^*}^* = 2[\mu] \bar{u}_{0_{x^*}}^* = \frac{1}{4} (\rho g \ell \epsilon) \exp \left[\frac{\sqrt{2/3}}{h^{*-}} \left(x^* + \frac{\ell}{2} \right) \right]. \quad (3.35a)$$

3.4. Downstream boundary layer

We note here that the dimensional stress in the *downstream* transition point, $x^* = \ell/2$ can be derived analogously. Similar to (3.28), the dimensionless surface profile in the boundary-layer region around the downstream transition point gives

$$h(x) = H^+ - \epsilon X' \quad \text{with} \quad H^+ = 1 - \lambda/2 \quad \text{and} \quad X' = (x - \lambda/2)/\epsilon, \quad (3.36)$$

where H^+ indicates the dimensionless ice thickness at the downstream transition point and X' is the local coordinate of the downstream boundary-layer region with the center at the downstream transition point. Then, the governing equation in the downstream boundary-layer region becomes

$$\underbrace{U_{X' X'} H^+}_{\text{extension}} - \underbrace{\frac{2U}{3H^+}}_{\text{shear}} = 0. \quad (3.37)$$

Anti-symmetric to (3.31) and (3.32), the boundary conditions for the downstream boundary layer is

$$\lim_{X' \rightarrow +\infty} U \approx 0 \quad \text{and} \quad U_{X'}(X' = 0) = -\frac{\lambda}{8}. \quad (3.38)$$

Combining equation (3.37) with the boundary conditions (3.38), the strain rate (and therefore also stress) within the downstream boundary-layer region is derived as

$$U_{X'} = -\frac{\lambda}{8} \exp \left[-\sqrt{\frac{2}{3}} \frac{X'}{H^+} \right]. \quad (3.39)$$

Recalling the horizontal length scale $[x_{bl}]$ (3.23) and velocity scale $[u_{bl}]$ (3.25) of the boundary layer, the expression of λ (3.4), H^+ and X' (3.36), the dimensional stress in the boundary-layer region at the downstream transition point is

$$\tau_{x^* x^*}^* = 2[\mu] \frac{[u_{bl}]}{[x_{bl}]} U_{X'} = -\frac{1}{4} (\rho g \ell \epsilon) \exp \left[\frac{-\sqrt{2/3}}{h^{**}} \left(x^* - \frac{\ell}{2} \right) \right], \quad (3.40a)$$

where $h^{**} = H^+ h_0 = h_0 - \ell \epsilon / 2$ is the dimensional ice thickness at the downstream transition point.

3.5. Summary of analytical solution

We here summarize our analytical solution for the stress response of the ice sheet to the presence of a slippery patch. We do so in a piece-wise manner, with one solution in the upstream boundary layer (3.40), one across the slippery patch (3.11), and the last one in the downstream boundary layers, which reads

$$\tau_{x^* x^*}^*(x^*) = \begin{cases} \frac{1}{4} \rho g \ell \epsilon \exp \left[\frac{\sqrt{2/3}}{h^{*-}} \left(x^* + \frac{\ell}{2} \right) \right] & \text{for } -O(h_0) \leq x^* + \frac{\ell}{2} \leq 0, \\ -\frac{1}{2} \rho g \epsilon x^* & \text{for } -\frac{\ell}{2} \leq x^* \leq \frac{\ell}{2}, \\ -\frac{1}{4} \rho g \ell \epsilon \exp \left[\frac{-\sqrt{2/3}}{h^{**}} \left(x^* - \frac{\ell}{2} \right) \right] & \text{for } 0 \leq x^* - \frac{\ell}{2} \leq O(h_0). \end{cases} \quad (3.41)$$

It is clear from (3.41) that the stresses at the transition points are proportional to the product of the surface slope ϵ and the length of the patch ℓ , and the decay lengthscale of the stress is proportional to the thickness at the upstream (-) and downstream (+) transition points, $h^{*\pm}$. The stress then decreases linearly across the length of the slippery patch. On the downstream side of the patch, the stress rebounds and returns exponentially to the far-field no-slip stress. This exposes an apparent structure to the controls on stress response wherein the ice surface slope and patch length control the magnitude and the ice thickness dictates the decay lengthscale (coupling length). Of note is the fact that the stress magnitude does not depend on the ice viscosity, rather it is governed by a pressure gradient $\rho g \ell \epsilon$ set by the thickness change across the length of the slippery patch. To further explore and confirm the results of this model, we turn to numerical simulations.

4. Numerical experiment results

While the analytical model (3.41) clearly demonstrates the result, in this section we present results from 2D numerical simulations in an effort to: (1) corroborate the results of the analytical model and (2) investigate the relationships between ice sheet geometry and stress response at the ice surface for both Newtonian and non-Newtonian rheologies. We ran a series

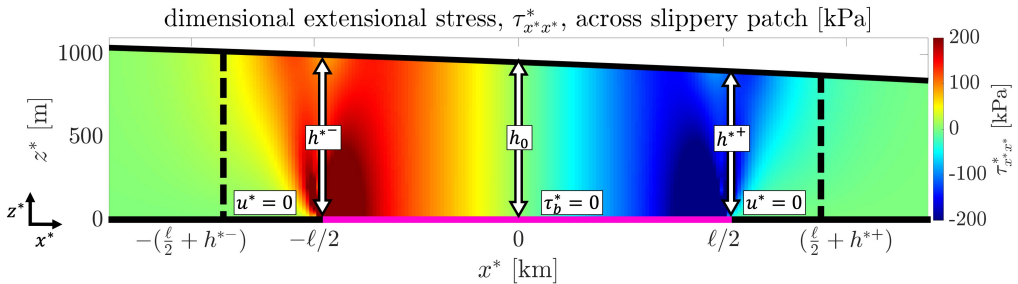


Figure 3: Dimensional example of model domain section for the numerical simulation with transition point thickness $h^{*-} = 1000\text{m}$, surface slope $\epsilon = 0.5^\circ$, and patch length $\ell = 10\text{km}$, showing the perturbation to the dimensional horizontal deviatoric stress $\tau_{x^*x^*}^*$ (red extension, blue compression) in response to the presence of a slippery patch (pink). The extent of the upstream and downstream boundary layers are indicated by the dashed vertical lines located at $x^* = -(\frac{\ell}{2} + h^{*-})$ and $x^* = (\frac{\ell}{2} + h^{*+})$, respectively.

of numerical experiments with Elmer/Ice (Gagliardini *et al.* 2013) with ice flowing over a flat bed characterized by no-slip everywhere except for a spatially-finite patch of free-slip (figure 3). Each experiment was set up such that we specified the combination of ice thickness and surface slope at the upstream end of the slippery patch, which also ranged in length. In particular, we used ice thicknesses of 750, 1000, and 1500 meters, surface slopes of 0.25° , 0.50° , and 0.75° , and patch lengths of 2, 5, 8, and 10 kilometers. These parameters were chosen to be consistent with realistic ice sheet slopes and thicknesses in regions with known basal meltwater lubrication and spanning a realistic range in estimated basal lubrication lateral extents (e.g., Stevens *et al.* 2015; Lai *et al.* 2021; Stevens *et al.* 2024). We note that in all cases, the patch is located sufficiently far away ($> 30h_0$) from the ice front as to avoid interfering stress interactions there. We repeated this set of simulations for a constant Newtonian viscosity ($\mu = 10^{14}$ Pa s), as well as for a non-Newtonian rheology, governed by Glen flow law rheology (4.1) (Glen 1955), for a total of 72 independent simulations. The surface topography of each simulation was set to be a solution to the classical viscous gravity current profile diffusion (appendix A), which were dimensionally-scaled to meet the thickness and surface slope specifications of the individual experiment.

We begin with a presentation of the results for ice with constant viscosity ($\mu = 1 \times 10^{14}$ Pa s) and show that these numerical results may be readily explained by the analytical model (§4.1). We then display the stress response for non-Newtonian ice viscosity (§4.2), which is more analogous to real-world glacial ice (e.g., Glen 1955). For both Newtonian and non-Newtonian rheologies, we include both surface and depth-averaged stresses, as the depth-averaged stresses are more directly comparable to our analytical model while surface stresses are more relevant to the motivating process of fracture formation / propagation on the GrIS surface.

4.1. Newtonian rheology

Inspection of the numerical results reveals an apparent self-similar structure to the patch-induced stress response. Namely, stress responses for different geometric parameter combinations (i.e., thickness, surface slope, patch length) are commonly characterized by a stress response that peaks near the transition point, decays upstream (left) away from the transition point, decreases nearly linearly from upstream to downstream (left to right) across the patch, reaches a minimum value near the downstream transition point, and returns exponentially to equilibrium on the downstream (right) end (figure 4). Proper non-dimensionalization of the depth-averaged numerical simulations and comparison to the analytical stress profile (3.41)

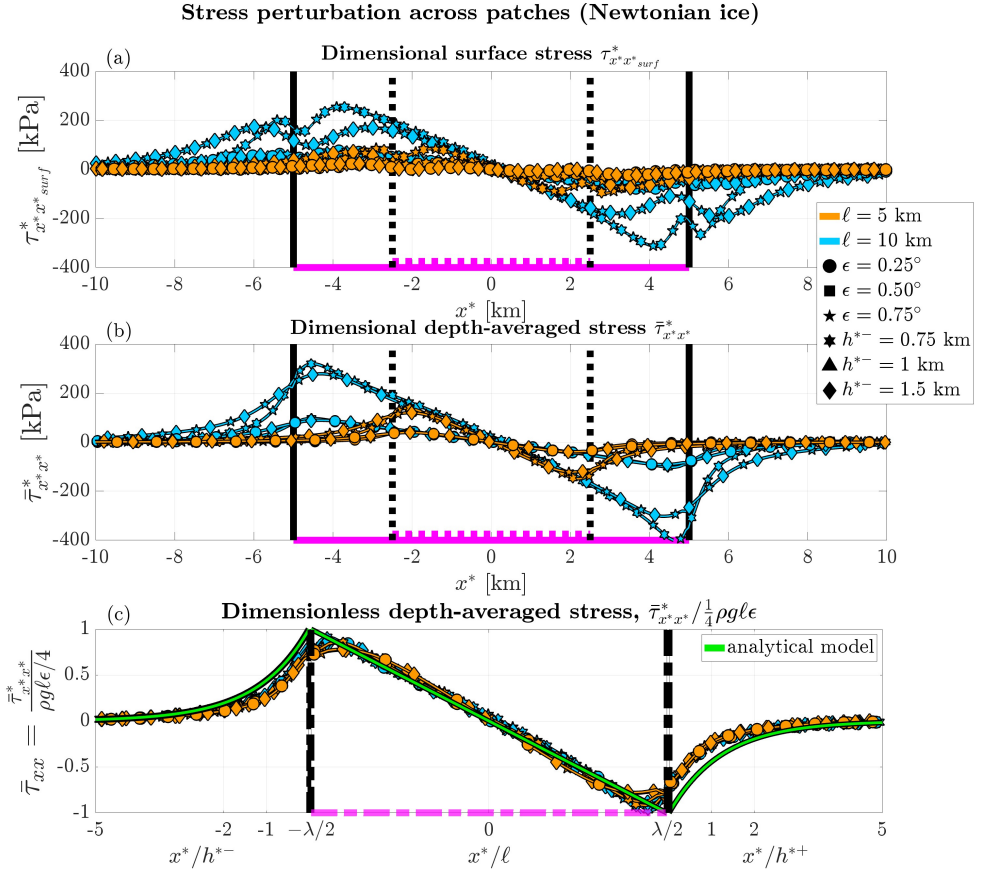


Figure 4: Horizontal deviatoric stress (surface at top, depth-averaged middle and rescaled depth-averaged at bottom) across slippery patch for a range of ice thicknesses, surface slopes, and patch lengths. Agreement between depth-averaged numerical and analytical models is displayed in the bottom plot.

reveals that our non-dimensional analytical model accurately captures these features of the stress (strain rate) response shape in the three regions: upstream, interior, and downstream of the patch (figure 4).

To further highlight the relationships discussed above across all numerical experiments, we extracted the following values (both depth-averaged and at the ice surface) from each model run: (1) maximum magnitude of extensional stress upstream (left) of the patch onset and (2) distance upstream from the transition point over which the extensional stress decays to $1/e$ of its maximum value, which we refer to as ‘coupling length’ (CL). We note here that the definition of coupling length is constructed to reflect the exponential nature of the stress response as elucidated by the analytical model, though the consequences of a different definition are discussed further in §5. Analysis of these stress quantities (magnitude, CL) reveals linear relationships between coupling length and ice thickness (figure 4a,d), between stress magnitude and surface slope (figure 4b,e), and between stress magnitude and patch length (figure 4c,f). These relationships are consistent with our analytical theory (section 2), where stress magnitude is a function of surface slope and patch length, and decay lengthscale is a function of ice thickness. It is notable that these relationships hold most strongly for cases where the ratio of patch length to ice thickness is notably greater than one. For example,

Relationships between geometry (h^{*-} , ϵ , ℓ) and stress response (CL, magnitude)

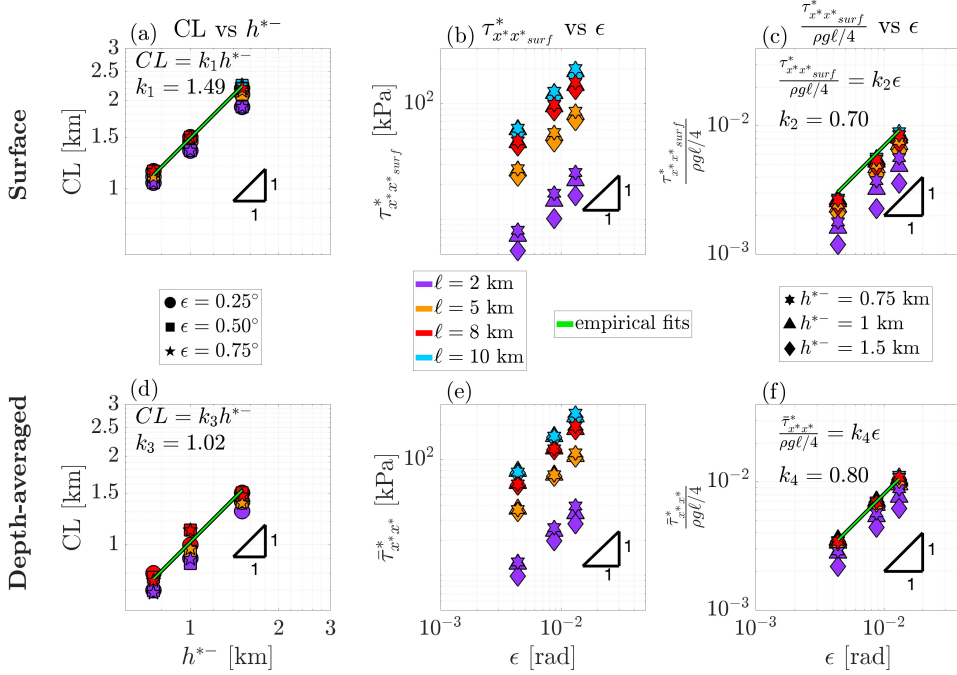


Figure 5: Relationships of coupling length to thickness (left), stress magnitude to surface slope (middle), and stress magnitude normalized by $\rho g \ell$ to surface slope (right) for surface (top row) and depth-averaged (bottom row) horizontal extensional stresses, τ_{xx} , in response to the presence of a slippery patch. Green fit lines represent the functional relationships which take into account only patch lengths equal to and above 5 km.

the collapse of data to a characteristic linear curve in figure 4f after being rescaled by patch length reveals that the stress magnitude has a linear dependence on the patch length for all but the cases with thickness nearing the length of the patch (purple diamonds: $h^{*-} = 1.5$ km, $\ell = 2$ km). Consistent with this observation, inspection of figure 4a also reveals the relationship between coupling length and thickness holds most strongly for cases with patch size much larger than the thickness. This limitation is reflected in both the depth-averaged stresses as well as the surface stresses (4c,f). While this limitation may appear to arise out of the numerical simulations, it is in fact consistent with the analytical model. As discussed previously (§3.1), our theory requires that $\epsilon \ll \lambda \ll [x]$, which implies $1 \ll \frac{\ell}{h_0} \ll \epsilon^{-1}$. Because we have treated this condition to be finite to leading order, the ratio of thickness to patch length must be greater than and not approach unity, otherwise this boundary condition vanishes to leading order. It is consistent then that we see a break-down of the theory in the limit where the patch length is smaller than or approaches to the ice thickness.

4.2. Non-Newtonian rheology

As ice sheets are characterized by a non-Newtonian, shear-thinning rheology (e.g., Glen 1955), we here extend the above numerical framework to consider an ice sheet with viscosity given by the so-called Glen flow law. This rheology is characterized by a power-law relationship between stress and strain rate, with a stress exponent of $n = 3$, which leads

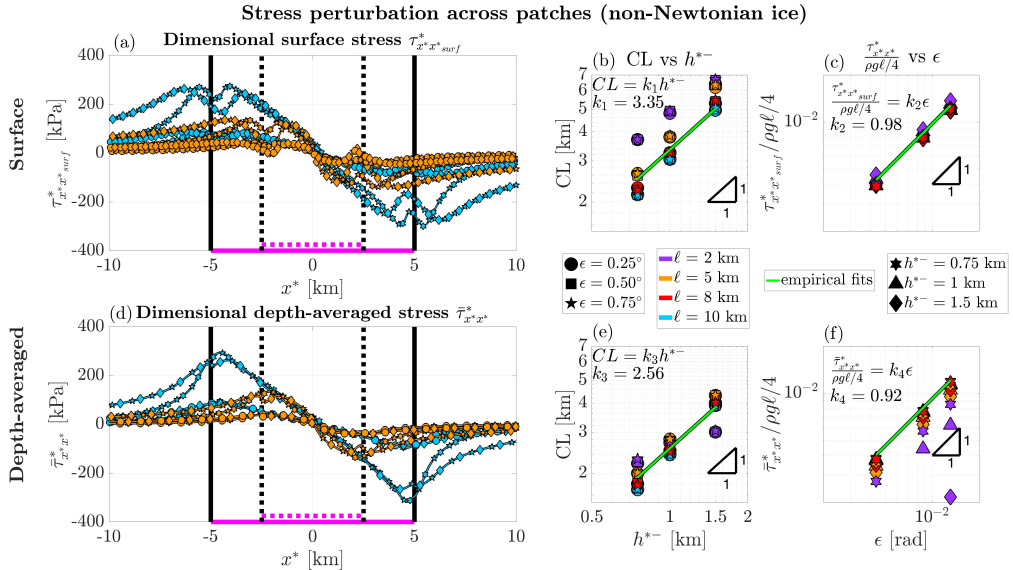


Figure 6: Same as figure 4 and 5, but for non-Newtonian (Glen law) rheology, showing stresses across the patches (surface (a) and depth-averaged (b)) as well as associated linear relationships between CL and thickness (b,e) and between stress magnitude and surface slope and patch length (c,f).

to a strain rate-dependent viscosity (4.1):

$$\dot{\epsilon}_e = A\tau_e^n, \quad (4.1a)$$

$$\tau_e = 2\mu\dot{\epsilon}_e, \quad (4.1b)$$

$$\Rightarrow \mu = \frac{1}{2}A^{\frac{1}{n}}(\dot{\epsilon}_e)^{\frac{n-1}{n}}, \quad (4.1c)$$

where we use a standard value for the prefactor, $A = 24 \times 10^{-25} \text{ Pa}^{-3} \text{ s}^{-1}$ (Cuffey & Paterson 2010). As with the Newtonian case, we extract the coupling length and stress magnitude from the range of simulations, and see the same qualitative relationships where coupling length is linearly controlled by the ice thickness and the surface slope linearly dictates the stress magnitude. The influence of the patch length is nearly perfectly linear for the surface stresses, while we see again our theory breaks down for experiments characterized by a patch length which approaches the ice thickness. This deviation from the dominant trend is further highlighted by the fact that the coupling length is not linearly dependent on the thickness for the case where the patch length is 2 km and the ice thickness is 1.5 km (purple markers, figure 6e).

4.3. Summary of numerical results

Our numerical experiments, including experiments with both of the chosen rheologies (Newtonian and non-Newtonian), maintain good agreement with the analytical model, which posits that the decay lengthscale (coupling length, CL) is linearly related to the local thickness while the magnitude of the stress perturbation is linearly related to the surface slope and patch length. These numerically-obtained linear relationships are summarized along with their associated pre-factors in table 1.

Surface		Depth-averaged	
$CL = k_1 h^{*-}$		$CL = k_3 h^{*-}$	
$\tau_{x^* x^*}^*_{surf} = k_2 \rho g \ell \epsilon / 4$		$\bar{\tau}_{x^* x^*}^* = k_4 \rho g \ell \epsilon / 4$	
Newtonian	Glen	Newtonian	Glen
$k_1 = 1.49$	$k_1 = 3.35$	$k_3 = 1.02$	$k_3 = 2.56$
$k_2 = 0.70$	$k_2 = 0.98$	$k_4 = 0.80$	$k_4 = 0.92$

Table 1: Summary of the relationships between ice sheet geometry and perturbed stress response as obtained from the numerical experiments.

5. Discussion

5.1. Summary of result and relationships with previous work

Motivated by seasonally-occurring rapid injections of meltwater to the ice-bed interface via GrIS supraglacial lake drainages, which occur when the ice reaches a requisite stress threshold, our goal in this work has been to reveal theoretical relationships between ice sheet geometry and the stress which responds to this basal lubrication. To seek a clear analytic expression of these relationships, our approach reduced the problem down to analyzing the stress response of an idealized viscous gravity current flowing over a spatially-finite shear-free patch. Inspired by analytical models derived in the prior studies (Schoof 2007b; Pegler 2016), we developed a new reduced-order boundary layer model framework. Despite describing different systems, the governing equations of these papers share similarities, as summarized in table 2. Pegler (2016) employs a leading-order balance among pressure, shear, and extension under a width-integrated approach to model a confined extensional flow, such as the flow of a confined floating ice shelf. Schoof (2007a) deals with the transition from shear-dominated (but allowed to slide) grounded to floating ice at the grounding line. This gives rise to a stress balance marked by a leading-order balance of pressure and shear and a higher-order contribution of extensional stresses, leading to a singular perturbation at the grounding line and necessitating a matched asymptotics approach to resolve the boundary layer structure in the flow. In addition to Schoof (2007a), Mantelli *et al.* (2019) also applied a boundary layer approach to the transition problem to analyze the dynamics very close to the transition point at the bed. A demonstration of the consistency between our numerical results and the analytical treatment of a switch in basal boundary condition from no-slip to free-slip by Mantelli *et al.* (2019) can be found in Appendix B.

In our work, we examine the stress perturbations associated with hard-switches on either end of a spatially-finite patch of free-slip surrounded by no-slip for fully grounded ice using matched asymptotics to resolve the perturbations in the boundary layers near the transition points. The novelty in this approach is the development of a new analytical reduced-order model derived from first principles under a matched asymptotics framework, revealing that the perturbed stress reaches an upstream maximum value proportional to the pressure drop across the patch, $\rho g \ell$, and decays exponentially upstream away from the transition point with a decay lengthscale proportional to the local ice thickness 3.41. The analytical model accurately describes the depth-averaged simulations (for cases where the patch size is much

Schoof (2007b), eq 2.12:	$\underbrace{-hh_x}_{\text{pressure}} - \underbrace{\bar{u}}_{\text{shear}} + 4\epsilon(h\bar{u}_x)_x = 0$
Pegler (2016), eq 3.4:	$\underbrace{-hh_x}_{\text{pressure}} - \underbrace{h\bar{u}}_{\text{shear}} + 4(\underbrace{h\bar{u}_x}_x) = 0$
Our work (no-slip):	$\underbrace{-hh_x}_{\text{pressure}} - \underbrace{3\frac{\bar{u}_0}{h}}_{\text{shear}} - \underbrace{\epsilon^2 \partial_z u_1 _b}_{O(\epsilon^2) \text{ shear}} + \underbrace{\frac{3}{2}\epsilon^2 [3(\bar{u}_{0_x}h)_x - (\bar{u}_0h_x)_x]}_{O(\epsilon^2) \text{ extension}} = 0$
Our work (free-slip):	$\underbrace{-hh_x}_{\text{pressure}} + 4(\underbrace{\bar{v}_{0_x}h}_x) = 0$

Table 2: Comparison of similar models by Schoof (2007a) and Pegler (2016), which consider a balance among pressure, shear, and extension. In the Schoof (2007b) model, $\epsilon = \epsilon^2$, where ϵ is the same as in our work. We show the Newtonian ($n = 1$) case of both models, where the notation of some variables is altered from the original source papers (e.g., added an overbar to the velocities, removed basal topography from the Schoof (2007a) model) to be more consistent with the notation used in our paper, for simplified comparison.

larger than the ice thickness, see §4.1), verifying the validity of the model and the insight therein: local fluid (ice) thickness linearly controls the coupling length while the surface slope and slippery patch length control the magnitude of stress perturbation. These relationships are seen beyond just the depth-averaged Newtonian cases, as the simulation-derived surface stresses for both the Newtonian and non-Newtonian rheology qualitatively reflect these dominant controls (figures 5, 6 and table 1).

The findings presented here agree well qualitatively with existing studies. Notably, the literature broadly agrees that the lateral extent of the viscous response of ice sheets to spatially-finite basal heterogeneities is on the order of several ice thicknesses (e.g., Kamb & Echelmeyer 1986; Barcilon & MacAyeal 1993; Gudmundsson 2003; Sergienko 2013; Mantelli *et al.* 2019). Our model also suggests this scaling, both via the numerical experiments (figures 5, 6) as well as the analytical model which necessitates an $O(h_0)$ rescaling of the inner boundary-layer (3.41). We find that the coupling length (length over which perturbed stress returns to $1/e$ of its peak value, see section 4) is on the order of several ice thicknesses. Our results reveal shorter coupling lengths ($\sim 1h^*$) for the Newtonian cases and longer ($\sim 3h^*$) for the non-Newtonian cases, indicating a dependence of stress coupling length on rheology (table 1). Interestingly, a similar behaviour was noted by Kamb & Echelmeyer (1986), who showed that the lengthscale of stress-gradient coupling related to longitudinal variations in basal topography was longer for non-Newtonian ice than for Newtonian ice.

The stress perturbation magnitudes are similar for the Newtonian and non-Newtonian cases, as is the scaling of magnitude to slope and patch length. Notably, there is good agreement between the depth-averaged analytical model with the full 2D Stokes flow simulations, with both Newtonian and non-Newtonian results characterized by stress perturbations of the same scale (e.g., figures 4, 6).

5.2. Implications for ice sheets

An open question facing the glaciology community is: how are stresses coupled between neighboring regions across the GrIS? The importance of this question stems from understanding how the ice sheet generally will respond to continued arctic warming (and therefore

meltwater forcing), with implications ranging from understanding the dynamics of summer lake-drainage-driven speed-up events (e.g., Zwally *et al.* 2002) to the hydrofracture cascade hypothesis (e.g., Christoffersen *et al.* 2018). For example, Zwally *et al.* (2002) observed an increase in summer ice surface velocities at a location ~ 40 km inland from the western GrIS margin (Swiss Camp), attributing this speed-up to the presence of meltwater at the ice-bed interface due to hydrofracture-driven lake drainage. It was later shown, however, that the speed-up observed at this location could be described by an alternative mechanism. Namely, Price *et al.* (2008) demonstrated that a seasonal acceleration near the coast (> 10 km downstream from the Swiss Camp location) may have caused the observed speed-up upstream at Swiss Camp.

The communication of stresses between lakes in response to their drainage is still yet to be fully constrained. It remains unclear precisely how and how far these stresses may be transmitted in response to the injection of meltwater to the bed. Modeling of membrane stress response to basal traction loss by Christoffersen *et al.* (2018) suggests there may be a mechanism by which lakes located several tens of kilometers apart may transmit stresses in a way such that one lake drainage can trigger another. Observations by Stevens *et al.* (2024) of elastic stresses generated by rapid lake drainages suggest an elastic stress-coupling length limited to the order of several ice thicknesses, or a few kilometers. In this study, our reduced-order viscous model (for justification of our choice of viscous rheology see Appendix C) indicates that, under our idealized conditions, stress coupling length is fundamentally limited to the scale of the ice thickness, even in the end-member cases of extreme basal boundary switch such as our no-slip to free-slip transitions. Furthermore, our work implies that the ice surface slope and the length of the slippery patch, not the ice thickness, dominantly controls the magnitude of the stress response, consistent with the observations of Stevens *et al.* (2024).

Though the stress coupling lengthscale is linearly proportional to the local ice thickness, the exponential nature of the stress response suggests that we should be particular in our definition of the term ‘coupling length’. If we are interested in the absolute extent over which the perturbed stress remains above a given value (as an illustrative example, we here use 30 kPa), then this extent is a function not only of the decay lengthscale but also the maximum magnitude of the stress perturbation which is a function of the local ice surface slope and patch length. The maximum stress magnitude, and therefore coupling length, are then unique functions of location on the ice sheet. From our depth-averaged analytical solution, we computed the maximum stress magnitude and coupling length (perturbed stress $\tau_{x^*x^*}^* \geq 30$ kPa) at each combination of surface slope and thickness, assuming a slippery patch length of 10 km. Projecting these values onto an example ice sheet profile reveals that locations further upstream experience smaller stress perturbations and shorter stress coupling extents 7. The location on an ice sheet, and the combination of surface slope and ice thickness thereof, dictate the stress response, which is generally more muted at locations further (inland) from the ice margin.

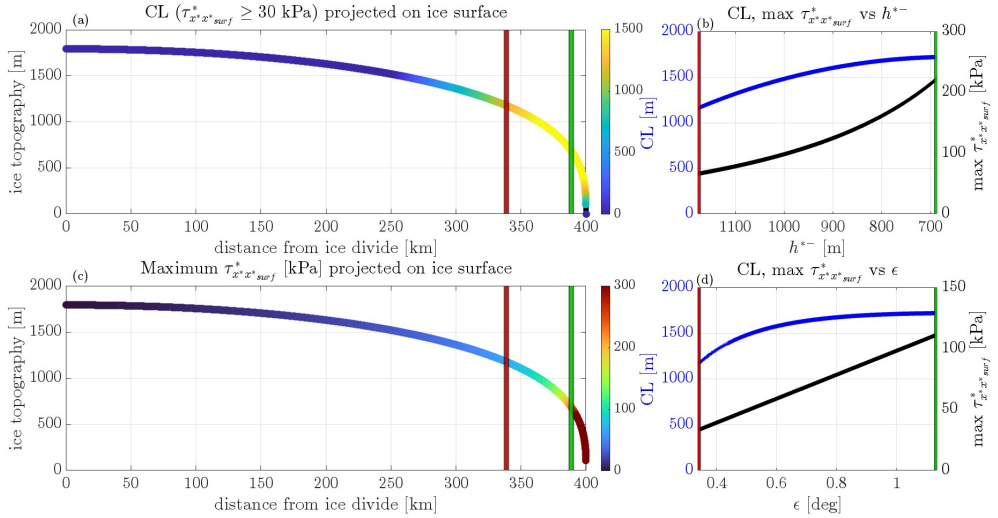


Figure 7: Stress magnitude and coupling extent from the depth-averaged model projected onto example of ice sheet surface profile (a, c). Stress and coupling length as functions of thickness (b) and surface slope (d).

Thus, though the presence of supraglacial lakes is expected to expand inland from the GrIS margin under the warming future climate (e.g., [Leeson *et al.* 2015](#)), these inland locations may be shielded from the same hydrofracture effects currently observed for lakes located closer to the margin. Stress perturbations may be of smaller magnitude (leading to shorter absolute coupling extents above a critical threshold, despite thicker ice) due to flatter surface slopes. Lakes then may be less likely to drain via hydrofracture, and ones that do drain may be less likely to trigger drainage cascades with nearby lakes. Further constraints on these likelihoods are necessary, especially as the inland subglacial system is believed to be more susceptible to basal traction loss in the presence of meltwater injection ([Schoof 2010](#); [Meierbachtol *et al.* 2013](#); [Dow *et al.* 2014](#); [Doyle *et al.* 2014](#); [Poinar *et al.* 2015](#)).

5.3. Future work

We note that this idealized framework remains not quantitatively representative of the whole process or thresholds that govern lake drainage or stress transmission on the GrIS. However, the simplicity of this framework has allowed us to theoretically uncover the fundamental mechanisms that govern the stress perturbations of an ice sheet due to basal lubrication. This may provide guidance in future work, for example, aimed at accurately resolving the conditions under which lake hydrofracture drainages or cascades might occur. Specifically, extending this framework to more realistic geometries (e.g., bed topography, local thickness gradients), rheologies (e.g., elastic / viscoelastic), realistic basal boundary conditions and time effects (e.g., ice advection, time-dependent basal hydrology coupling) would enhance the realism and comparability of the model to observations. Our work serves as an opportunity for comparison between observations / realistic models and the simplified finding that surface slope and ice thickness have distinct, but related, effects on the stress response of an idealized ice sheet, treated as a viscous gravity current, to the presence of a meltwater-induced basal slippery patch.

Acknowledgements

We thank O. Gagliardini (University of Grenoble Alpes) for the helpful advice on Elmer/Ice simulations.

Funding statement

The authors acknowledge partial support from NSF's Office of Polar Programs through OPP-2344690.

Declaration of interests

Competing interests: The authors report no conflicts of interest.

Author ORCIDs

Joshua H. Rines: <https://orcid.org/0000-0002-3743-1096>

Ching-Yao Lai: <https://orcid.org/0000-0002-6552-7546>

Yongji Wang: <https://orcid.org/0000-0002-3987-9038>

Author contributions

Conceptualization: J.H.R. and C.-Y. L.; Formal Analysis: J.H.R., Y. W., C.-Y. L.; Funding acquisition: C.-Y. L.; Writing – original draft: J.H.R.; Writing – review and editing: J.H.R., Y. W., C.-Y. L.

Appendix A. Non-newtonian viscous gravity current surface profile derivation

In this appendix, we present the derivation of the ice surface topography used for the Elmer/Ice simulations, the shape of which varies noticeably depending on choice of rheology (e.g., Newtonian vs. non-Newtonian). Beginning with a dimensional version of the Stokes equations (2.2), and assuming we have a shear-dominated flow (e.g., no-slip basal boundary condition), we have the so-called Shallow Ice Approximation (SIA):

$$-\rho g \partial_x h + \partial_z (\mu \partial_z u) = 0, \quad (\text{A } 1)$$

which is subjected to the following boundary conditions:

$$u(z = 0) = 0 \quad (\text{A } 2a)$$

$$\partial_z u|_{z=h} = 0. \quad (\text{A } 2b)$$

For a power-law viscosity, given by:

$$\mu = \frac{B}{2} (\dot{\epsilon}_e)^{\frac{n-1}{n}} \quad (\text{A } 3)$$

where $\dot{\epsilon}_e = \frac{1}{2} \partial_z u$ to leading-order, we determine the velocity profile by simple integration:

$$u(x, z, t) = \frac{2}{n+1} \left(-\frac{\rho g}{B} \partial_x h \right)^n [h^{n+1} - (h-z)^{n+1}]. \quad (\text{A } 4)$$

We note here that $B = A^{1/n}$, where A is the common notation used for the Arrhenius prefactor for Glen law rheology (e.g., section 4.2, equation 4.1). Substitution of the velocity profile

(A 4) into the incompressible thickness equation (A 5):

$$\partial_t h + \partial_x \left(\int_0^h u dz \right) = 0, \quad (\text{A } 5)$$

yields the classic nonlinear diffusion equation which governs the evolution of the ice gravity current profile:

$$\partial_t h + \partial_x \left[C h^{n+2} \left(1 - \frac{1}{n+2} \right) \right] = 0, \quad (\text{A } 6)$$

where the constant, $C = \frac{2}{n+1} \left(-\frac{\rho g}{B} \partial_x h \right)^n$. This nonlinear partial differential equation for the diffusion of thickness h (A 6) may be solved by recognizing self-similarity of the system, which reduces (A 6) from a PDE requiring three boundary conditions to an ODE requiring only two boundary conditions: (1) vanishing thickness at the fluid front (A 7a) and (2) global mass continuity (A 7b)

$$h(L) = 0 \quad (\text{A } 7a)$$

$$\int_0^{x_N(t)} h(x, t) dx = q t^\alpha, \quad (\text{A } 7b)$$

where q is a constant and α varies depending on the fluid input scheme. In our case, we assume a constant volume, setting $\alpha = 0$. To solve the nonlinear diffusion PDE (A 6), we first establish characteristic scales for the thickness and horizontal dimensions, h_0 and x_0 , respectively, by inspection of (A 6) and (A 7b):

$$h_0 = Q J^{-1} t^\xi \quad (\text{A } 8a)$$

$$x_0 = q Q^{-1} J t^{-\xi}, \quad (\text{A } 8b)$$

where $Q = q^{\frac{n+1}{3n+2}}$, $J = \left[\frac{2}{n+1} \left(\frac{\rho g}{B} \right)^n \left(1 - \frac{1}{n+2} \right) \right]^{\frac{1}{3n+2}}$, and $\xi = -\frac{1}{3n+2}$ are constants.

Taking the standard similarity solution ansatz, we assume the solution for the fluid thickness, h , may be written in the form $h(x, t) = h_0 f(\eta)$, where $\eta = x/x_0$. Substitution into (A 6) yields:

$$Q J^{-1} t^{\xi-1} [\xi f - f' \eta (-\xi)] + J^{-1} Q^{(3n+2)} q^{-(n+1)} t^{(3\xi)(n+1)} (f^{(n+2)} (-f')^n)' = 0, \quad (\text{A } 9)$$

which, after recognizing the exponential equivalence of each term, allows us to write the key ODE we aim to solve in an integrable form:

$$\begin{aligned} & [\xi f - f' \eta \xi] + \left[f^{(n+2)} (-f')^n \right]' = 0, \\ & \Rightarrow \xi (f \eta)' + (f^{(n+2)} (-f')^n)' = 0 \end{aligned} \quad (\text{A } 10)$$

where the apostrophe denotes the derivative with respect to our similarity variable, η (e.g., $f' = \partial_\eta f$). The associated boundary conditions for vanishing ice front thickness (A 7a) and global continuity (A 7b) likewise become:

$$h_0 f(\eta_{front}) = 0 \Rightarrow f(\eta_{front}) = 0 \quad (\text{A } 11a)$$

$$\int_0^{\eta_f} f(\eta) d\eta = 1, \text{ where } \eta_f = \eta_{front} = \frac{x_f}{q Q^{-1} J t^{-\xi}}, \quad (\text{A } 11b)$$

Before solving, we elect to rescale the ODE (A 10) and the boundary conditions (A 11) for independent variable, $s \equiv \eta/\eta_f$, and dependent variable, $g \equiv f/\eta_f^{\frac{2}{n+2}}$, to fit the solution between 0 and 1, leaving us with the following system of ODE (A 12) and boundary conditions

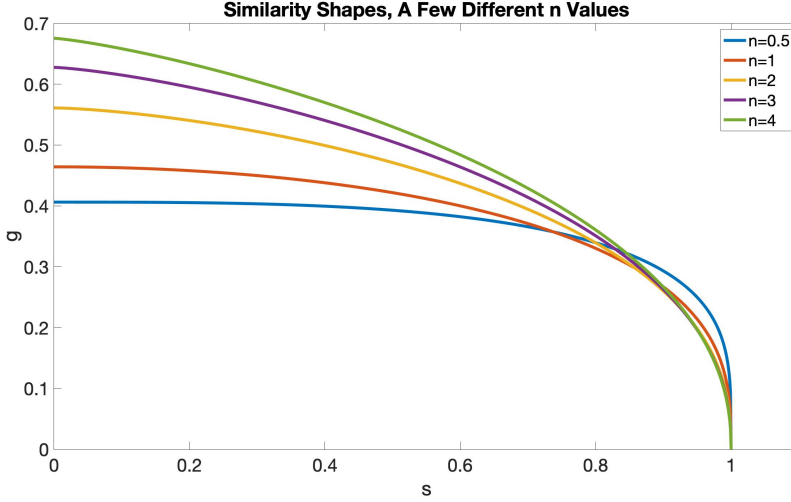


Figure 8: Non-dimensional viscous gravity current profiles for $n=0.5, 1, 2, 3, 4$.

(A 13):

$$\left(-\frac{1}{3n+2}\right)(sg)' + ((-g')^n g^{(n+2)})' = 0 \quad (\text{A 12})$$

$$g(1) = 0 \quad (\text{A 13a})$$

$$\int_0^1 \eta_f^{\frac{n+4}{2}} g ds = 1, \quad (\text{A 13b})$$

Solution of this closed ODE system is now a matter of simple integration, yielding the nondimensional similarity solution for the gravity-driven evolution of the ice surface (figure 8):

$$g(s) = \left[\left(\frac{1}{3n+2} \right)^{\frac{1}{n}} \left(\frac{n}{n+1} \right) \right]^{\left(\frac{n}{2n+1} \right)} \left[1 - s \left(\frac{n+1}{n} \right) \right]^{\left(\frac{n}{2n+1} \right)} \quad (\text{A 14})$$

In our numerical experiments (section 4), we simply re-dimensionalize the horizontal dimension of these profiles such that their ice front is 400 km away from the ice divide, and re-dimensionalize the vertical dimension in such a way to enforce the desired ice thickness and surface slope combination at the onset of the slippery patch.

Appendix B. Numerical comparison to Mantelli *et al.* (2019)

Though Mantelli *et al.* (2019) focuses on elucidating the thermomechanical feedbacks within a flow system subjected to a single hard-switch in basal boundary condition from no-slip to free-slip, we note the horizontal velocity in their mechanical model (B 1, equation 15i of their supplement) is analogous to our system:

$$u_{(M19)} \sim -\frac{c}{2} R^{1/2} \left[-5 \cos \left(\frac{\theta}{2} \right) + \cos \left(\frac{3\theta}{2} \right) \right], \quad (\text{B 1})$$

where they solved for the horizontal velocity, u , in a small region near the patch onset as a function of distance, R , and azimuth angle, θ , away from the hard-switch point. In

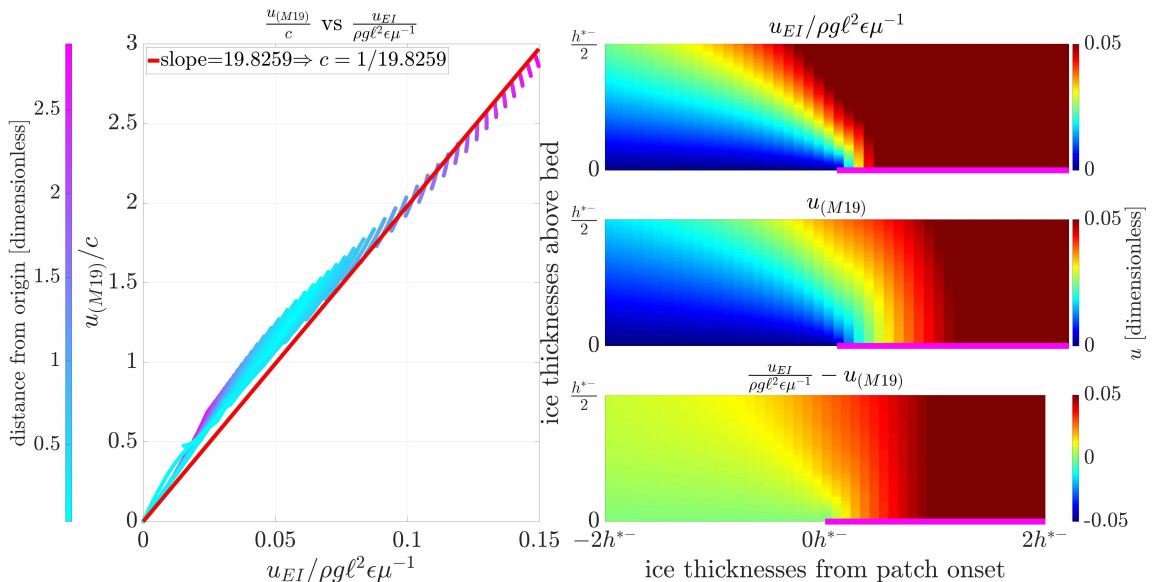


Figure 9: Comparison between the analytical solution to the mechanical model from [Mantelli *et al.* \(2019\)](#), $u_{(M19)}$, (right, middle) and the non-dimensionalized horizontal velocity field from our Elmer/Ice simulations, $u_{EI}/\rho g \ell^2 \epsilon \mu^{-1}$, (right, top). The small relative difference between the two fields (bottom) demonstrates the similarity between models. The panel on the left demonstrates the process for empirically determining the scaling factor, c , from [Mantelli *et al.* \(2019\)](#), determined here to be $c = 39.4$. The numerical experiment used for this comparison was the case with $h^{*-} = 1000$ m, $\epsilon = 0.5^\circ$, and patch length $l = 5000$ m, where the slippery patch is depicted by the pink line at the ice-bed interface in each frame.

particular the analytical solution to this mechanical model bears striking resemblance to the numerical simulations we produced using Elmer/Ice (figure 9). As [Mantelli *et al.* \(2019\)](#) point out, c is a scaling factor which is determined via matching with the far field. In the illustrative example above, we have empirically-fit a scaling factor of $c = 39.4$, which leads to a compelling similarity between our numerical simulations and the analytical mechanical model of [Mantelli *et al.* \(2019\)](#).

Appendix C. Timescales of viscous relaxation

A notable difference between the assumptions of our model and those of existing models is that we do not explicitly assume a steady-state. Namely, we do not consider a situation where the system has evolved to re-equilibrate to the presence of the basal heterogeneity. We recognize that the appearance of a slippery patch would, over time, lead to an expression in the ice surface topography. However, we consider a case where the slippery patch is present at the ice-bed interface for a long enough time to consider the system to be a viscous fluid, but short enough to neglect surface adjustment effects, as we only consider a single topography configuration. A simple scaling argument based on the thickness evolution equation demonstrates that this can be the case, using typical ice sheet values of $h_0 = 10^3$ m, $[v] = 1000$ m/yr, $[x] = 10^4$ m:

$$\partial_t h + \partial_x (uh) = 0 \quad (\text{C } 1a)$$

$$\Rightarrow h_0/[t] \sim [v][h]/[x] \quad (\text{C } 1b)$$

$$\Rightarrow h_0/[t] \sim 2 \text{ m/week}, \quad (\text{C } 1c)$$

which is on the order of 0.2% thickness change during the course of a week, over which a slippery patch to be present. With the Maxwell timescale for ice on the order of one day, this puts us comfortably in a middle ground where we can justify the use of a viscous framework which exists over a short enough timescale that the deformation of the ice will be negligible, and thus allows us to consider a single (time-independent, though not steady-state) ice topography geometry. As we have a fixed surface topography, it either applies to places where the surface topography does not adjust quickly to the changes in basal topography (scaling argument) or to places where the accumulation/ablation scheme is such that the surface topography does not change over time. While this is an oversimplification, it allows us to develop this framework, which may be qualitatively looked for in real data or more realistic models.

REFERENCES

- ALLEY, RICHARD B., DUPONT, TODD K., PARIZEK, BYRON R. & ANANDAKRISHNAN, SRIDHAR 2005 Access of surface meltwater to beds of sub-freezing glaciers: preliminary insights. *Annals of Glaciology* **40**, 8–14.
- BARCILON, VICTOR & MACAYEAL, DOUGLAS R. 1993 Steady flow of a viscous ice stream across a no-slip/free-slip transition at the bed. *Journal of Glaciology* **39** (131), 167–185, publisher: Cambridge University Press.
- BARTHOLOMEW, I. D., NIENOW, P., SOLE, A., MAIR, D., COWTON, T., KING, M. A. & PALMER, S. 2011 Seasonal variations in Greenland Ice Sheet motion: Inland extent and behaviour at higher elevations. *Earth and Planetary Science Letters* **307** (3), 271–278.
- BINDSCHADLER, ROBERT & VORNBERGER, PATRICIA 1998 Changes in the West Antarctic Ice Sheet Since 1963 from Declassified Satellite Photography. *Science* **279** (5351), 689–692, publisher: American Association for the Advancement of Science.
- BUELER, ED, LINGLE, CRAIG, BROWN, JED, COVEY, DAVID & BOWMAN, LATRICE 2005 Exact solutions and verification of numerical models for isothermal ice sheets. *Journal of Glaciology* **51**, 291–306.
- CHRISTOFFERSEN, POUL, BOUGAMONT, MARION, HUBBARD, ALUN, DOYLE, SAMUEL H., GRIGSBY, SHANE & PETERSSON, RICKARD 2018 Cascading lake drainage on the Greenland Ice Sheet triggered by tensile shock and fracture. *Nature Communications* **9** (1), 1064.
- CHUGUNOV, VLADIMIR A. & WILCHINSKY, ALEXANDER V. 1996 Modelling of a marine glacier and ice-sheet-ice-shelf transition zone based on asymptotic analysis. *Annals of Glaciology* **23**, 59–67.
- CLARKE, GARRY K. C., NITSAN, UZI & PATERSON, W. S. B. 1977 Strain heating and creep instability in glaciers and ice sheets. *Reviews of Geophysics* **15** (2), 235–247, eprint: <https://onlinelibrary.wiley.com/doi/pdf/10.1029/RG015i002p00235>.
- CROZIER, JOSH, KARLSTROM, LEIF & YANG, KANG 2018 Basal control of supraglacial meltwater catchments on the Greenland Ice Sheet. *The Cryosphere* **12** (10), 3383–3407, publisher: Copernicus GmbH.
- CUFFEY, KURT & PATERSON, W. S. B. 2010 *The Physics of Glaciers: Fourth Edition*. Academic Press.
- DAS, SARAH B., JOUGHIN, IAN, BEHN, MARK D., HOWAT, IAN M., KING, MATT A., LIZARRALDE, DAN & BHATIA, MAYA P. 2008 Fracture Propagation to the Base of the Greenland Ice Sheet During Supraglacial Lake Drainage. *Science* **320** (5877), 778–781, publisher: American Association for the Advancement of Science.
- DOW, C. F., KULESSA, B., RUTT, I. C., DOYLE, S. H. & HUBBARD, A. 2014 Upper bounds on subglacial channel development for interior regions of the Greenland ice sheet. *Journal of Glaciology* **60** (224), 1044–1052, publisher: Cambridge University Press.
- DOYLE, SAMUEL H., HUBBARD, ALUN, FITZPATRICK, ANDREW A. W., VAN AS, DIRK, MIKKELSEN, ANDREAS B., PETERSSON, RICKARD & HUBBARD, BRYN 2014 Persistent flow acceleration within the interior of the Greenland ice sheet. *Geophysical Research Letters* **41** (3), 899–905, eprint: <https://onlinelibrary.wiley.com/doi/pdf/10.1002/2013GL058933>.
- FITZPATRICK, A. A. W., HUBBARD, A. L., BOX, J. E., QUINCEY, D. J., VAN AS, D., MIKKELSEN, A. P. B., DOYLE, S. H., DOW, C. F., HASHOLT, B. & JONES, G. A. 2014 A decade (2002–2012) of supraglacial lake volume estimates across Russell Glacier, West Greenland. *The Cryosphere* **8** (1), 107–121, publisher: Copernicus GmbH.
- FOWLER, A. C., LARSON, D. A. & FRANK, FREDERICK CHARLES 1978 On the flow of polythermal glaciers

- I. Model and preliminary analysis. *Proceedings of the Royal Society of London. A. Mathematical and Physical Sciences* **363** (1713), 217–242, publisher: Royal Society.
- GAGLIARDINI, O., ZWINGER, T., GILLET-CHAULET, F., DURAND, G., FAVIER, L., DE FLEURIAN, B., GREVE, R., MALINEN, M., MARTÍN, C., RÅBACK, P., RUOKOLAINEN, J., SACCHETTINI, M., SCHÄFER, M., SEDDIK, H. & THIES, J. 2013 Capabilities and performance of Elmer/Ice, a new-generation ice sheet model. *Geoscientific Model Development* **6** (4), 1299–1318, publisher: Copernicus GmbH.
- GLEN, J. W. 1955 The creep of polycrystalline ice. *Proceedings of the Royal Society of London. Series A. Mathematical and Physical Sciences* **228** (1175), 519–538, publisher: Royal Society.
- GUDMUNDSSON, G. HILMAR 2003 Transmission of basal variability to a glacier surface. *Journal of Geophysical Research: Solid Earth* **108** (B5).
- HALFAR, P. 1981 On the dynamics of the ice sheets. *Journal of Geophysical Research* **86** (C11), 11065.
- HEWITT, I.J. 2013 Seasonal changes in ice sheet motion due to melt water lubrication. *Earth and Planetary Science Letters* **371–372**, 16–25.
- HINDMARSH, RICHARD C. A. 1990 Time-scales and degrees of freedom operating in the evolution of continental ice-sheets. *Earth and Environmental Science Transactions of The Royal Society of Edinburgh* **81** (4), 371–384, publisher: Royal Society of Edinburgh Scotland Foundation.
- HULBE, C. & FAHNESTOCK, M. 2007 Century-scale discharge stagnation and reactivation of the Ross ice streams, West Antarctica. *Journal of Geophysical Research: Earth Surface* **112** (F3), [_eprint: https://onlinelibrary.wiley.com/doi/pdf/10.1029/2006JF000603](https://onlinelibrary.wiley.com/doi/pdf/10.1029/2006JF000603).
- HUPPERT, HERBERT E. 1982 The propagation of two-dimensional and axisymmetric viscous gravity currents over a rigid horizontal surface. *Journal of Fluid Mechanics* **121** (-1), 43.
- HUTTER, KOLUMBAN 1983 *Theoretical Glaciology*. publisher: Springer Dordrecht.
- IGNÉCZI, ÁDÁM, SOLE, ANDREW J., LIVINGSTONE, STEPHEN J., LEESON, AMBER A., FETTWEIS, XAVIER, SELMES, NICK, GOURMELEN, NOEL & BRIGGS, KATE 2016 Northeast sector of the Greenland Ice Sheet to undergo the greatest inland expansion of supraglacial lakes during the 21st century. *Geophysical Research Letters* **43** (18), 9729–9738, [_eprint: https://onlinelibrary.wiley.com/doi/pdf/10.1002/2016GL070338](https://onlinelibrary.wiley.com/doi/pdf/10.1002/2016GL070338).
- JOUGHIN, I., DAS, S. B., FLOWERS, G. E., BEHN, M. D., ALLEY, R. B., KING, M. A., SMITH, B. E., BAMBER, J. L., VAN DEN BROEKE, M. R. & VAN ANGELEN, J. H. 2013 Influence of ice-sheet geometry and supraglacial lakes on seasonal ice-flow variability. *The Cryosphere* **7** (4), 1185–1192.
- JOUGHIN, IAN, DAS, SARAH B., KING, MATT A., SMITH, BEN E., HOWAT, IAN M. & MOON, TWILA 2008 Seasonal Speedup Along the Western Flank of the Greenland Ice Sheet. *Science* **320** (5877), 781–783, publisher: American Association for the Advancement of Science.
- KAMB, BARCLAY & ECHELMAYER, KEITH A. 1986 Stress-Gradient Coupling in Glacier Flow: I. Longitudinal Averaging of the Influence of Ice Thickness and Surface Slope. *Journal of Glaciology* **32** (111), 267–284, publisher: Cambridge University Press.
- LAI, CHING-YAO, STEVENS, LAURA A., CHASE, DANIELLE L., CREYTS, TIMOTHY T., BEHN, MARK D., DAS, SARAH B. & STONE, HOWARD A. 2021 Hydraulic transmissivity inferred from ice-sheet relaxation following Greenland supraglacial lake drainages. *Nature Communications* **12** (1), 3955, number: 1 Publisher: Nature Publishing Group.
- LEESON, A. A., SHEPHERD, A., BRIGGS, K., HOWAT, I., FETTWEIS, X., MORLIGHEM, M. & RIGNOT, E. 2015 Supraglacial lakes on the Greenland ice sheet advance inland under warming climate. *Nature Climate Change* **5** (1), 51–55, number: 1 Publisher: Nature Publishing Group.
- LEUNG, LUCAS TSUN-YIN & KOWAL, KATARZYNA N. 2022 Lubricated viscous gravity currents of power-law fluids. Part 1. Self-similar flow regimes. *Journal of Fluid Mechanics* **940**, A26, publisher: Cambridge University Press.
- MACAYEAL, DOUGLAS R. 1989 Large-scale ice flow over a viscous basal sediment: Theory and application to ice stream B, Antarctica. *Journal of Geophysical Research: Solid Earth* **94** (B4), 4071–4087.
- MACAYEAL, DOUGLAS R. & BARCLON, VICTOR 1988 Ice-shelf Response to Ice-stream Discharge Fluctuations: I. Unconfined Ice Tongues. *Journal of Glaciology* **34** (116), 121–127, publisher: Cambridge University Press.
- MACFERRIN, M., MACHGUTH, H., AS, D. VAN, CHARALAMPIDIS, C., STEVENS, C. M., HEILIG, A., VANDECURX, B., LANGEN, P. L., MOTTRAM, R., FETTWEIS, X., BROEKE, M. R. VAN DEN, PFEFFER, W. T., MOUSSAVI, M. S. & ABDALATI, W. 2019 Rapid expansion of Greenland's low-permeability ice slabs. *Nature* **573** (7774), 403–407, number: 7774 Publisher: Nature Publishing Group.
- MANTELLI, E., HASELOFF, M. & SCHOOF, C. 2019 Ice sheet flow with thermally activated sliding. Part 1:

- the role of advection. *Proceedings. Mathematical, Physical, and Engineering Sciences* **475** (2230), 20190410.
- MEIERBACHTOL, T., HARPER, J. & HUMPHREY, N. 2013 Basal Drainage System Response to Increasing Surface Melt on the Greenland Ice Sheet. *Science* **341** (6147), 777–779, publisher: American Association for the Advancement of Science.
- MORLAND, L. W. 1987 Unconfined Ice-Shelf Flow. In *Dynamics of the West Antarctic Ice Sheet* (ed. C. J. Van der Veen & J. Oerlemans), *Glaciology and Quaternary Geology*, pp. 99–116. Dordrecht: Springer Netherlands.
- MORLAND, L. W. & JOHNSON, I. R. 1980 Steady Motion of Ice Sheets. *Journal of Glaciology* **25** (92), 229–246, publisher: Cambridge University Press.
- NYE, J. F. 2000 A flow model for the polar caps of Mars. *Journal of Glaciology* **46** (154), 438–444, publisher: Cambridge University Press.
- PEGLER, SAMUEL S. 2016 The dynamics of confined extensional flows. *Journal of Fluid Mechanics* **804**, 24–57.
- POINAR, KRISTIN & ANDREWS, LAUREN C. 2021 Challenges in predicting Greenland supraglacial lake drainages at the regional scale. *The Cryosphere* **15** (3), 1455–1483, publisher: Copernicus GmbH.
- POINAR, KRISTIN, JOUGHIN, IAN, DAS, SARAH B., BEHN, MARK D., LENAERTS, JAN T. M. & VAN DEN BROEKE, MICHEL R. 2015 Limits to future expansion of surface-melt-enhanced ice flow into the interior of western Greenland. *Geophysical Research Letters* **42** (6), 1800–1807, _eprint: <https://onlinelibrary.wiley.com/doi/pdf/10.1002/2015GL063192>.
- PRICE, S. F., PAYNE, A. J., CATANIA, G. A. & NEUMANN, T. A. 2008 Seasonal acceleration of inland ice via longitudinal coupling to marginal ice. *Journal of Glaciology* **54** (185), 213–219, publisher: Cambridge University Press.
- RIGNOT, E., MOUGINOT, J. & SCHEUCHL, B. 2011 Ice Flow of the Antarctic Ice Sheet. *Science* **333** (6048), 1427–1430, publisher: American Association for the Advancement of Science.
- RINK, HENRY 1877 *Danish Greenland: Its People and its Products*. publisher: Henry S. King & Co.
- SCHOOF, CHRISTIAN 2007a Ice sheet grounding line dynamics: Steady states, stability, and hysteresis. *Journal of Geophysical Research: Earth Surface* **112** (F3), _eprint: <https://onlinelibrary.wiley.com/doi/pdf/10.1029/2006JF000664>.
- SCHOOF, CHRISTIAN 2007b Marine ice-sheet dynamics. Part 1. The case of rapid sliding. *Journal of Fluid Mechanics* **573**, 27–55.
- SCHOOF, CHRISTIAN 2010 Ice-sheet acceleration driven by melt supply variability. *Nature* **468** (7325), 803–806, number: 7325 Publisher: Nature Publishing Group.
- SCHOOF, CHRISTIAN 2012 Marine ice sheet stability. *Journal of Fluid Mechanics* **698**, 62–72, publisher: Cambridge University Press.
- SERGIENKO, OLGA V. 2013 Glaciological twins: basally controlled subglacial and supraglacial lakes. *Journal of Glaciology* **59** (213), 3–8, publisher: Cambridge University Press.
- SOLE, ANDREW, NIENOW, PETER, BARTHOLOMEW, IAN, MAIR, DOUGLAS, COWTON, THOMAS, TEDSTONE, ANDREW & KING, MATT A. 2013 Winter motion mediates dynamic response of the Greenland Ice Sheet to warmer summers. *Geophysical Research Letters* **40** (15), 3940–3944, _eprint: <https://onlinelibrary.wiley.com/doi/pdf/10.1002/grl.50764>.
- STEVENS, LAURA A., BEHN, MARK D., DAS, SARAH B., JOUGHIN, IAN, NOËL, BRICE P. Y., VAN DEN BROEKE, MICHEL R. & HERRING, THOMAS 2016 Greenland Ice Sheet flow response to runoff variability. *Geophysical Research Letters* **43** (21), 11295–11303, _eprint: <https://onlinelibrary.wiley.com/doi/pdf/10.1002/2016GL070414>.
- STEVENS, LAURA A., BEHN, MARK D., MCGUIRE, JEFFREY J., DAS, SARAH B., JOUGHIN, IAN, HERRING, THOMAS, SHEAN, DAVID E. & KING, MATT A. 2015 Greenland supraglacial lake drainages triggered by hydrologically induced basal slip. *Nature* **522** (7554), 73–76, number: 7554 Publisher: Nature Publishing Group.
- STEVENS, LAURA A., DAS, SARAH B., BEHN, MARK D., MCGUIRE, JEFFREY J., LAI, CHING-YAO, JOUGHIN, IAN, LAROCHELLE, STACY & NETTLES, MEREDITH 2024 Elastic Stress Coupling Between Supraglacial Lakes. *Journal of Geophysical Research: Earth Surface* **129** (5), e2023JF007481, _eprint: <https://onlinelibrary.wiley.com/doi/pdf/10.1029/2023JF007481>.
- STUBBLEFIELD, AARON G., SPIEGELMAN, MARC & CREYTS, TIMOTHY T. 2021 Variational formulation of marine ice-sheet and subglacial-lake grounding-line dynamics. *Journal of Fluid Mechanics* **919**, A23, publisher: Cambridge University Press.

- SWITHINBANK, C. W. M. 1954 "Ice streams". *Polar Record* **7** (48), 185–186, publisher: Cambridge University Press.
- VENULEO, SARA, POKRAJAC, DUBRAVKA, SCHLEISS, ANTON J. & FRANCA, MÁRIO J. 2019 Continuously-fed gravity currents propagating over a finite porous substrate. *Physics of Fluids* **31** (12), 126601.
- VAN DE WAL, R. S. W., BOOT, W., VAN DEN BROEKE, M. R., SMEETS, C. J. P. P., REIJMER, C. H., DONKER, J. J. A. & OERLEMANS, J. 2008 Large and Rapid Melt-Induced Velocity Changes in the Ablation Zone of the Greenland Ice Sheet. *Science* **321** (5885), 111–113.
- WEERTMAN, J. 1957 Deformation of Floating Ice Shelves. *Journal of Glaciology* **3** (21), 38–42, publisher: Cambridge University Press.
- WEERTMAN, J. 1974 Stability of the Junction of an Ice Sheet and an Ice Shelf. *Journal of Glaciology* **13** (67), 3–11, publisher: Cambridge University Press.
- YUEN, DAVID A. & SCHUBERT, GERALD 1979 The Role of Shear Heating in the Dynamics of Large Ice Masses. *Journal of Glaciology* **24** (90), 195–212, publisher: Cambridge University Press.
- ZWALLY, H. JAY, ABDALATI, WALEED, HERRING, TOM, LARSON, KRISTINE, SABA, JACK & STEFFEN, KONRAD 2002 Surface Melt-Induced Acceleration of Greenland Ice-Sheet Flow. *Science* **297** (5579), 218–222.